Probing the Magnetic Anisotropy of Co(II) Complexes Featuring Redox-Active Ligands

Journal:	*Inorganic Chemistry*
Manuscript ID	ic-2020-01812g.R1
Manuscript Type:	Article
Date Submitted by the Author:	10-Sep-2020
Complete List of Authors:	Kumar, Praveen; Marquette University, Chemistry SantaLucia, Daniel; University of Wisconsin Madison, Department of Chemistry Kaniewska-Laskowska, Kinga; Politechnika Gdanska, Lindeman, Sergey; Marquette University, Department of Chemistry Ozarowski, Andrew; Florida State University, Natl High Magnet Field Lab Krzystek, Jurek; Florida State University, National High Magnetic Field Laboratory Ozerov, Mykhaylo; National High Magnetic Field Laboratory Telser, Joshua; Roosevelt University, Biological, Chemical and Physical Sciences Berry, John; University of Wisconsin Madison, Department of Chemistry Fiedler, Adam; Marquette University, Chemistry

SCHOLARONE™
Manuscripts

Probing the Magnetic Anisotropy of Co(II) Complexes Featuring Redox-Active Ligands

Praveen Kumar,[†,#] Daniel J. SantaLucia,[§,#] Kinga Kaniewska-Laskowska,[⊗]

Sergey V. Lindeman,[†] Andrew Ozarowski,[⊥] J. Krzystek,[⊥] Mykhaylo Ozerov,[⊥]

Joshua Telser,[◇] John F. Berry,*,[§] and Adam T. Fiedler*,[†]

# P.K. and D.J.S. contributed equally

† Department of Chemistry, Marquette University, Milwaukee, Wisconsin 53201, United States

§ Department of Chemistry, University of Wisconsin – Madison, Madison, Wisconsin 53706, United States

⊗ Department of Inorganic Chemistry, Faculty of Chemistry, Gdańsk University of Technology, Gdańsk PL-80-233, Poland.

⊥ National High Magnetic Field Laboratory, Florida State University, Tallahassee, Florida 32310, United States

◇ Department of Biological, Chemical and Physical Sciences, Roosevelt University, Chicago, Illinois 60605, United States

Email contact: adam.fiedler@marquette.edu (A.T.F), berry@chem.wisc.edu (J.F.B.)

Fax number: (+1) 414-288-7066

Abstract

Coordination complexes that possess large magnetic anisotropy (otherwise known as zero-field splitting, ZFS) have possible applications in the field of magnetic materials, including single molecule magnets (SMMs). Previous studies have explored the role of coordination number and geometry in controlling the magnetic anisotropy and SMM behavior of high-spin ($S = 3/2$) Co(II) complexes. Building upon these efforts, the present work examines the impact of ligand oxidation state and structural distortions on the spin states and ZFS parameters of pentacoordinate Co(II) complexes. The five complexes included in this study (**1-5**) have the general formula, $[Co(Tp^{Ph2})(L^{X,Y})]^{n+}$ (X = O, S; Y = N, O; n = 0 or 1), where Tp^{Ph2} is the scorpionate ligand hydrotris(3,5-diphenyl-pyrazolyl)borate(1−) and $L^{X,Y}$ are bidentate dioxolene-type ligands that can access multiple oxidation states. The specific $L^{X,Y}$ ligands used herein are 4,6-di-*tert*-butyl substituted *o*-aminophenolate and *o*-aminothiophenolate (**1** and **2**, respectively), *o*-iminosemiquinonate and *o*-semiquinonate radicals (**3** and **4**, respectively), and *o*-iminobenzoquinone (**5**). Each complex exhibits a distorted trigonal bipyramidal geometry, as revealed by single-crystal X-ray diffraction. Direct current magnetic susceptibility experiments confirmed that the complexes with closed-shell ligands (**1**, **2**, and **5**) possess $S = 3/2$ ground-states with negative D-values (easy-axis anisotropy) of −41, −78, and –29 cm^{-1}, respectively. For **3** and **4**, antiferromagnetic coupling between the Co(II) center and *o*-(imino)semiquinonate radical ligand results in $S = 1$ ground states that likewise exhibit very large and negative anisotropy ($-100 > D > -130$ cm^{-1}). Notably, ZFS was measured directly for each complex using far-infrared magnetic spectroscopy (FIRMS). In combination with high-frequency and -field electron paramagnetic resonance (HFEPR) studies, these techniques provided precise spin-Hamiltonian parameters for complexes **1**, **2**, and **5**. Multireference *ab initio* calculations, using the CASSCF/NEVPT2 approach, indicate that the strongly negative anisotropies of these Co(II) complexes arise primarily from distortions in the equatorial plane due to constrictions imposed by the Tp^{Ph2} ligand. This effect is further amplified by cobalt(II)-radical exchange interactions in **3** and **4**.

I. Introduction

The ability to measure and adjust the magnetic anisotropy of first-row transition metal complexes with $S > 1/2$ is critical to the development of cost-effective magnetic materials.[1-3] Magnetic anisotropy arises primarily from relativistic spin-orbit coupling (SOC) interactions that remove the degeneracy of the m_S-sublevels of the ground-state spin manifold even when an external magnetic field is absent.[4-5] This phenomenon – referred to as zero-field splitting (ZFS) – is generally described using a traceless **D**-tensor that consists of axial (D) and rhombic (E) terms. For molecules with axial symmetry ($E = 0$), negative anisotropy ($D < 0$) generates a doubly-degenerate ground state consisting of the largest m_S components ($+m_S$ and $-m_S$). The energy barrier for interconversion between the degenerate $\pm m_S$-levels slows the rate of magnetic relaxation, giving rise to bistability at low temperatures. This behavior is the basis of single-molecule magnets (SMMs),[6-9] which have potential applications in data storage, quantum computing, and spintronics technologies.[10-11] In general, the performance of SMMs is enhanced by increasing the absolute value of the axial D-term, while also minimizing the rhombic E-term that facilitates tunneling between $\pm m_S$ states.[12] Thus, the rational design of magnetic materials requires a detailed understanding of the geometric and electronic factors that determine the ZFS parameters of transition-metal complexes.

High-spin cobalt(II) complexes are attractive SMM candidates due to their half-integer spins ($S = 3/2$) and sizable magnetic anisotropy arising from SOC among ligand-field states.[13-17] Indeed, numerous studies have examined the impact of coordination number, molecular geometry, and ligand identity on the ZFS parameters and magnetic relaxation rates of mononuclear Co(II) complexes, as summarized in recent reviews.[18-21] Less explored is the ability of redox active ligands to modulate the magnetic anisotropy of Co(II)-based molecules. Changes in ligand oxidation state are expected to perturb the intrinsic anisotropy of Co(II) ions, and the presence of ligand-based radicals generates a "ladder" of different spin states via exchange interactions. While the valence tautomerism of six-coordinate cobalt-semiquinonate complexes has been studied extensively,[22-25] efforts to develop transition-metal SMMs consisting of one or more radical ligands also show promise.[26-33] The most common approach in this direction has employed radicals as bridging ligands between paramagnetic centers to create multimetallic complexes with large total spin (S_{tot}) values. A similar strategy uses radical ligands as organic linkers in metal-organic frameworks (MOFs) that combine magnetic and microporous properties.[34-38] Strong

exchange coupling between a given metal and ligand radical has been shown to facilitate slow magnetic relaxation by discouraging quantum tunneling and increasing the energy gap between the ground and excited states.[27,39] In addition to these benefits, redox-noninnocent ligands capable of undergoing reversible redox events could serve as "on-off" switches for SMM behavior.[40-41]

The present work examines the magnetic anisotropy of a series of five-coordinate Co(II) complexes that feature redox-active ligands in varying oxidation and spin states. As illustrated in Scheme 1, complexes **1**-**5** have the general formula $[Co^{II}(Tp^{Ph2})(L^{X,Y})]^{n+}$, where Tp^{Ph2} is the tridentate "scorpionate" ligand, hydrotris(3,5-diphenylpyrazol-1-yl)borate and $L^{X,Y}$ is a bidentate dioxolene-type ligand (X = O, S; Y = O, N; n = 0 or 1). The noninnocent nature of these $L^{X,Y}$ ligands has been well-established in studies of coordination complexes and metalloenzyme active sites.[42-45] These high-spin Co(II) complexes share similar distorted trigonal-bipyramidal coordination geometries, as revealed by X-ray crystallography. Notably, complexes **1, 3**, and **5** comprise a redox series in which the $L^{O,N}$ ligand exists in three distinct oxidation states: o-aminophenolate ($L^{O,N}$, closed-shell anion), o-iminosemiquinonate ($L^{O,N}_{ISQ}$, S = 1/2 radical), and o-iminobenzoquinone ($L^{O,N}_{IBQ}$, neutral closed-shell), respectively. Analogous complexes containing o-aminothiophenolate ($L^{S,N}$ in **2**) and o-semiquinonate radical ($L^{O,O}_{SQ}$ in **4**) ligands are included to assess the impact of different donor atoms on the electronic structure. Due to the inherent challenges in studying complexes with large magnetic anisotropy and ligand-based radicals, multiple techniques are employed to determine the spin-Hamiltonian parameters of **1**-**5**, including variable-temperature dc magnetometry and high-frequency and -field electron paramagnetic resonance (HFEPR) spectroscopy.[46-47] Most importantly, we also report direct and unambiguous measurements of magnetic anisotropy made through analysis of each complex with far-infrared magnetic spectroscopy (FIRMS).[48-49] The large and negative anisotropies directly observed for complexes **1**-**5** are rationalized on the basis of magneto-structural correlations developed using multiconfigurational *ab initio* calculations.
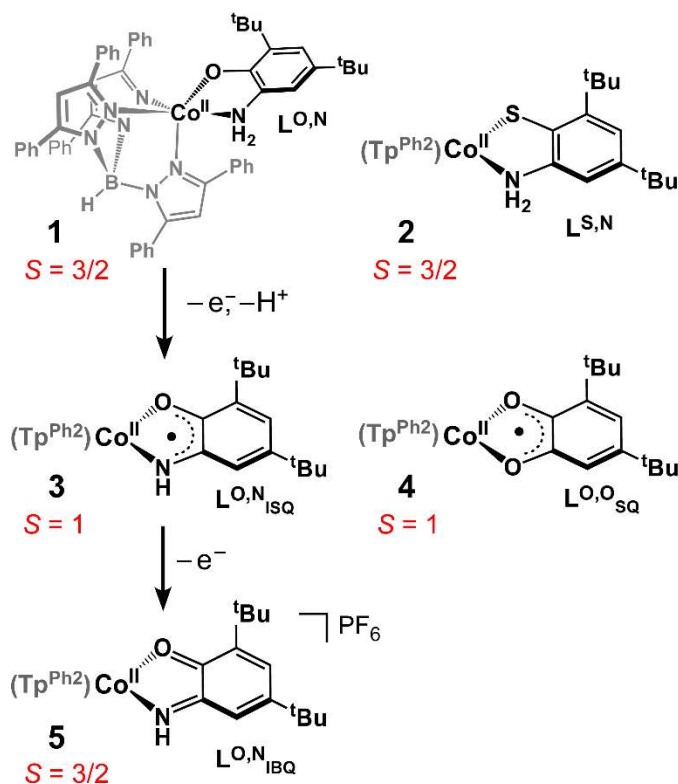
Scheme 1.

II. Experimental and Computational Methods

Materials and General Methods. Reagents and solvents were purchased from commercial sources and used without further purification unless stated otherwise. The syntheses and handling of the Co(II) complexes were carried out under an inert atmosphere using a Vacuum Atmospheres Omni-Lab glovebox equipped with a −30 ºC freezer. Solvents were deoxygenated prior to use and stored over molecular sieves in the glovebox. The compounds K(^{Ph2}Tp),[50] 4,6-di-*tert*-butyl-2-aminophenol,[51] [Co(Tp^{Ph2})(OAc)(Hpz^{Ph2})][52], and 4,6-di-*tert*-butyl-2-aminothiophenol[53] were prepared according to published procedures. We previously reported the syntheses of complexes **1** and **3**.[54] Elemental analysis data were collected at Midwest Microlab, LLC in Indianapolis, IN. UV-vis absorption spectra were measured in solution with an Agilent 8453 diode array spectrometer and IR spectra of solid-state samples were obtained with a Thermo Scientific Nicolet iS5 FTIR spectrometer. ^{1}H NMR spectra were measured using a Varian 400 MHz spectrometer.

Synthesis of [Co^{II}(Tp^{Ph2})(L^{S,N})] (2). Sodium methoxide (33 mg, 0.61 mmol) and 4,6-di-*tert*-butyl-2-aminothiophenol (120 mg, 0.51 mmol) were dissolved in THF (2 mL) and stirred for 30 minutes. Evaporation of the solvent provided a yellow residue that was combined with a solution

of [Co(Tp^{Ph2})(OAc)(Hpz^{Ph2})] (540 mg, 0.51 mmol) in CH$_2$Cl$_2$ (4 mL). The resulting mixture was stirred for two hours, followed by removal of the solvent under vacuum. A red solid was afforded and then extracted with Et$_2$O (2 × 5 mL). The combined extracts were filtered through Celite and dried under vacuum to give the crude product. Red-brown prisms of **2**, suitable for X-ray crystallographic analysis, were obtained by layering a concentrated CH$_2$Cl$_2$ solution with CH$_3$CN. Yield = 302 mg (61%). Anal. Calcd for C$_{59}$H$_{56}$BCoN$_7$S (M_W = 964.95 g mol^{-1}): C, 73.44; H, 5.85; N, 10.16; Found: C, 74.41; H, 5.95; N, 10.28. UV-vis [λ_{max}, nm (ε, M^{-1}cm^{-1}) in CH$_2$Cl$_2$]: 356 (1530), 439 (650), 500 (680), 1000 (50). ^{1}H NMR (400 MHz, CDCl$_3$): δ = 78.5 (*s*, 1H), 53.5 (*s*, 1H), 53.0 (*s*, 9H, -C(C*H*$_3$)$_3$), 49.4 (*s*, 3H, 4-*H*-pz), 28.0 (*s*, 6H, Tp-Ph-*H*), 17.9 (*s*, 6H, Tp-Ph-*H*), 14.8 (*s*, 3H, Tp-Ph-*H*), 10.1 (*s*, 1H), 5.75 (*s*, 6H, Tp-Ph-*H*), 4.6 (*s*, 3H, Tp-Ph-*H*), −3.95 (*s*, 9H, -C(C*H*$_3$)$_3$), −40.5 (*s*, 6H, Tp-Ph-*H*) ppm. μ_{eff} = 4.21 μ_B (Evans method in CDCl$_3$).

Synthesis of [Co^{II}(Tp^{Ph2})(L$^{O,O}_{SQ}$)] (4). To a vial containing NaOMe (45 mg, 0.83 mmol) and 3,5-di-*tert*-butylcatechol (91 mg, 0.41 mmol), [Co(Tp^{Ph2})(OAc)(H-pz^{Ph2})] (437 mg, 0.41 mmol) was added in a 3:1 mixture of CH$_2$Cl$_2$:MeOH (10 mL total). The brown mixture slowly turned dark green over the course of 16 hours while stirring, signaling generation of the **L$^{O,O}_{SQ}$** ligand. The solvent was removed *in vacuo* and the resulting solid was redissolved in Et$_2$O before filtration through Celite. The filtrate was placed in a −30 °C freezer, leading to formation of green X-ray quality crystals. After removal of the mother liquor, the crystalline product was washed once with hexanes and dried to give a green powder. Yield = 295 mg (74%). Anal. Calcd for C$_{59}$H$_{54}$BCoN$_6$O$_2$ (M_W = 948.86 g mol^{-1}): C, 74.68; H, 5.74; N, 8.86. Found: C, 74.67; H, 5.59; N, 8.77. UV-vis [λ_{max}, nm (ε, M^{-1}cm^{-1}) in CH$_2$Cl$_2$]: 370 (1070), 430 (1040), 575 (310), 615 (330), 740 (390). ^{1}H NMR (400 MHz, CDCl$_3$): δ = 85.4 (*s*, 1H), 53.5 (*s*, 1H), 35.6 (*s*, 3H, 4-*H*-pz), 26.6 (*s*, 6H, Tp-Ph-*H*), 16.9 (*s*, 6H, Tp-Ph-*H*), 14.3 (*s*, 3H, Tp-Ph-*H*), 9.3 (*s*, 3H, Tp-Ph-*H*), 7.6 (*s*, 6H, Tp-Ph-*H*), 7.0 (*s*, 1H), 0.5 (*s*, 9H, -C(C*H*$_3$)$_3$), −5.6 (*s*, 9H, -C(C*H*$_3$)$_3$), −42.4 (*s*, 6H, Tp-Ph-*H*). μ_{eff} = 2.68 μ_B (Evans method in CDCl$_3$).

Synthesis of [Co^{II}(^{Ph2}Tp)(L$^{O,N}_{IBQ}$)]PF$_6$ (5). [Co^{II}(Tp^{Ph2})(L$^{O,N}_{ISQ}$)] (**3**; 257 mg, 0.27 mmol) was dissolved in CH$_2$Cl$_2$ (5 mL) to yield a dark green solution. Treatment with AgPF$_6$ (68 mg, 0.27 mmol) resulted in an immediate color change to reddish-brown. The mixture was stirred for one hour and then filtered through Celite. The volume of the filtrate was reduced by half under vacuum, layered with CH$_3$CN, and placed in a −30 °C freezer. The crystals that formed after three days were harvested and dried to provide the red product. Yield = 198 mg (61%). Crystals for

crystallographic analysis were prepared by vapor diffusion of Et_2O into a concentrated solution of **5** in 1,2-dichloroethane. Anal. Calcd for $C_{59}H_{55}BCoF_6N_7OP$ (M_W = 1092.85 g mol^{-1}): C, 64.84; H, 5.07; N, 8.97; F, 10.43. Found: C, 65.75; H, 5.39; N, 8.95; F, 9.50. The discrepancy in the fluorine value is due to small amounts of a low-spin Co(II) impurity, as observed by HFEPR spectroscopy. UV-Vis [λ_{max}, nm (ε, M^{-1}cm^{-1}) in CH_2Cl_2]; 475 (2750), 580 (1800). ^1H NMR (400 MHz; $CDCl_3$): δ = 71.6 (s, 1H), 66.2 (s, 3H, 4-H-pz), 47.2 (s, 1H), 10.7 (s, 2 × 6H, Tp-Ph-H), 9.2 (s, 6H, Tp-Ph-H), 8.5 (s, 3H, Tp-Ph-H), 7.6 (s, 3H, Tp-Ph-H), 7.1 (s, 9H, -C(CH_3)$_3$), −3.1 (br s, 6H, Tp-Ph-H), −9.1 (s, 9H, -C(CH_3)$_3$). ^{19}F NMR (400 MHz; $CHCl_3$) δ = −61 ppm (d, J = 750 Hz). μ_{eff} = 4.49 μ_B (Evans method in $CDCl_3$).

X-ray Crystal Structure Determination. Single-crystal X-ray diffraction intensities from crystals of complexes **2**, **4**, and **5** were measured at 100 K with an Oxford Diffraction (Rigaku Corporation) SuperNova diffractometer. The instrument has dual-wave micro-focus sealed-tube sources (Cu and Mo K$_\alpha$ wavelengths), X-ray mirror optics, an Atlas CCD detector, and an open-flow Cryojet LN$_2$ cooling device (Oxford Instruments). In all cases Cu K$_\alpha$ radiation was used. The data were corrected for usual experimental factors including absorption correction based on the real shape of the crystals followed by a polynomial empirical procedure within the CrysAlis Pro (Rigaku, 2018) program package. The structures were solved using charge-flipping[55] and intrinsic phasing methods, then refined utilizing an anisotropic approximation for non-hydrogen atoms in a least-squares procedure.[56] Hydrogen atoms were positioned geometrically and a riding/rotating model was applied during refinement. A solvent-mask procedure was used to account for electron density of non-localized solvent molecules in the structure of **2**. The experimental parameters are summarized in Table S1. Crystallographic data (CIF) can be obtained from the Cambridge Crystallographic Data Centre under the deposition numbers 2009204 (**2**), 2009205 (**4**), and 2009206 (**5**).

Magnetic Susceptibility and Reduced Magnetization Experiments and Analysis. Variable-temperature paramagnetic susceptibility data and reduced magnetization data for complexes **1**-**5** were measured with a MPMS 3 Quantum Design SQUID magnetometer at the University of Wisconsin-Madison. Plots of the original susceptibility data are provided in Figures S1 (**1**), S4 (**2**), S8 (**3**), S11 (**4**), and S16 (**5**). The samples were cooled down in the absence of a magnetic field to 1.8 K and data were subsequently collected from 1.8 K to either 300 K or 400 K in an applied 1000 G DC magnetic field. Reduced-magnetization data (Figures S3(**1**), S6(**2**), S10

and Figure 3 (**3**), S14(**4**), and S19(**5**)) were also collected for each complex, at temperatures of 2, 4, 6, and 8 K for complexes **1**, **2**, and **5** and 2, 4, and 8 K for **3** and **4**. At each temperature, the field was varied from 0 to 7 T while measuring the magnetization of the sample. The 2 K dataset was excluded for the fitting of complex **2** due to a discontinuity in the data (Figure S6). Modeling the reduced magnetization data simultaneously with the susceptibility data was successful for complexes **3**, **4**, and **5** (Figures 3, S14, and S19, respectively); however, only the models for **3** and **5** were physically reasonable. Attempts to model the reduced magnetization data for **1** and **2** simultaneously with the susceptibility data were not successful and fitting the magnetization data individually led to physically unreasonable results (Figures S3 and S6, respectively). The simultaneous magnetization and susceptibility fit for **5** led to the same parameters, within error, as fitting the susceptibility data individually (Figures S17 and S19), but with greater precision; thus, the results obtained from the simultaneous fitting of the susceptibility and reduced magnetization data are reported in Table 1. All magnetic susceptibility and magnetization data were modeled using the fitting program PHI v.3.1.5.[57] Data for complexes **1-3** and **5** were parameterized using the following general form for the spin Hamiltonian:

$$\widehat{H} = \sum_i \beta \vec{S}_i \boldsymbol{g}_i \vec{H} + \sum_i \vec{S}_i \boldsymbol{D}_i \vec{S}_i$$

where β is the Bohr magneton, $\vec{H}$ is the applied external magnetic field, and $\vec{S}_i$, $\boldsymbol{g}_i$, and $\boldsymbol{D}_i$ are the spin vector, electronic **g**-tensor, and single-ion ZFS tensor for a given spin center, respectively. The first term of the spin Hamiltonian accounts for magnetic Zeeman interactions of the electron spins with an applied field while the second accounts for single-ion anisotropy (due to ZFS) for each spin center.[58] The **g**-tensors were modeled with axial components, $g_∥ = g_z$; $g_⊥ = g_x = g_y$. The use of rhombic g-values did not improve the quality of the fits. Therefore, only the axial g-value fits are reported in the main text, as these avoid overparameterization of the models, while the rhombic g-value fits are reported in the SI (see Figures S2, S5, S10, S12 and S18). The ZFS tensors, **D**, were modeled with axial (D) and rhombic (E) components. The susceptibility data for **3** and **4** were modeled including an extra isotropic exchange term in the spin Hamiltonian to account for antiferromagnetic coupling between the two spin centers in the compound. The Heisenberg-Dirac-Van Vleck exchange Hamiltonian operator was used. It is given by: $\widehat{H}_{ex} = -2J_{AB}\vec{S}_A\vec{S}_B$, where positive and negative values for J_{AB} correspond to ferromagnetic and antiferromagnetic coupling, respectively, between two spin centers $\vec{S}_A$ and $\vec{S}_B$.

Experimental susceptibility and magnetization data were corrected for inherent diamagnetism with the equation: $\chi_D = -(M_W/2) \cdot 10^{-6}$ cm^3 mol^{-1}.[59] For complexes **1**, **2**, **4**, and **5**, the temperature-independent magnetism (TIM, defined below) was included as a variable in the model of the susceptibility data, while for complex **3**, the slope of a linear least squares fit line of the last four high-temperature data points (at $T = 199$, 220, 244, and 271 K) in the $\chi_P \cdot T$ vs. T plot was used for the TIM correction (Figure S9). This manually-obtained TIM correction was included as a fixed parameter for modeling the data for **3** (Figures 2 and S10) because a refinable TIM parameter led to overcorrection in which values of $\chi_P \cdot T$ decreased instead of leveling off in the high-temperature regime.

Due to strong antiferromagnetic coupling between the Co(II) center and $\mathbf{L^{O,N}_{ISQ}}$ radical, complex **3** was modeled as an effective $S = 1$ spin center following the general form of the spin-Hamiltonian above. In contrast, **4** was modeled as two antiferromagnetically coupled spin centers, $S_{Co} = 3/2$ and $S_{SQ} = 1/2$, where the **g**-tensor of the $\mathbf{L^{O,O}_{SQ}}$ radical was fixed at $g_{iso} = 2.00$. After the parameters were obtained from modeling the susceptibility data for complex **3** (and deconvoluted with Clebsch-Gordan spin projection), they were used as fixed parameters in simulations to establish an upper limit for the isotropic exchange coupling constant (Figure S15). Two separate sets of fits were conducted on the susceptibility data for **4**; one set included the TIM parameter in the model (Figures 2 and S12), while the other excluded the TIM parameter (Figure S13). Because no good fits could be obtained using rhombic g-values while excluding the TIM parameter from the model, only the axial g-value fit is reported in the SI (Figure S13). The fit excluding the TIM parameter for **4** is inconsistent with the D parameter obtained by FIRMS and thus is deemed less physically reasonable.

FIRMS and HFEPR Studies. HFEPR experiments were performed using a transmission spectrometer described elsewhere[60] modified by the use of Virginia Diodes Inc. (VDI, Charlottesville, VA) sources, generating sub-THz wave radiation in a 50–640 GHz frequency range. The spectrometer is associated with a 15/17-T warm-bore superconducting magnet. FIRMS experiments were performed at the National High Magnetic Field Laboratory using a Bruker Vertex 80v FT-IR spectrometer coupled with a 17 T vertical-bore superconducting magnet in a Voigt configuration (light propagation perpendicular to the external magnetic field). The experimental setup employs broadband terahertz radiation emitted by an Hg arc lamp. The radiation transmitted through the sample is detected by a composite silicon bolometer (Infrared

Laboratories) mounted at the end of the quasi-optical transmission line. Both the sample and bolometer are cooled by low-pressure helium gas to a temperature of 4.6 K. The spectral intensity of each microcrystalline powder sample ($\sim$7 mg) bonded by *n*-eicosane were measured in the region between 14 and 730 cm^{-1} (0.42−22 THz) with a resolution of 0.3 cm^{-1} (9 GHz). To discern the magnetic absorptions, the spectra were normalized by dividing with the reference spectrum, which is the average spectrum for all magnetic fields. Such normalized transmittance spectra are only sensitive to intensity changes induced by the magnetic field and therefore are not obscured by nonmagnetic vibrational absorption features. The data analysis was implemented using an in-house written MATLAB code and the EPR simulation software package EasySpin.[61]

Computational Methods. Calculations were carried out using the ORCA software package (version 4.0) developed by Dr. F. Neese (MPI-CEC).[62-63] Computational models of **1-5** were based on the crystallographic structures, although the *tert*-butyl groups were replaced with methyl groups. The Tp^{Ph2} ligand was truncated by replacing the three 5-phenyl substituents with H-atoms to generate a Tp^{Ph,H} chelate. Two different Karlsruhe basis sets were employed: (i) valence double-ζ basis set with polarization functions (def2-SVP), and (ii) valence triple-ζ basis set combined with polarization functions on main-group and transition-metal elements (def2-TZVP).[64] Single point calculations of the truncated crystallographic structures employed Becke's three-parameter hybrid functional for exchange and the Lee-Yang-Parr correlation functional (B3LYP).[65-66] The resolution of identity and chain of sphere (RIJCOSX) approximations[67] were applied in conjunction with the appropriate auxiliary basis sets.[68] The unrestricted natural orbitals provided by the DFT/B3LYP calculations served as the initial guess for state-averaged CASSCF calculations. The core orbitals were not frozen. For the $S = 3/2$ complexes (**1**, **2**, and **5**), the CAS(7,5) active space consisted of seven electrons in the five Co 3d orbitals. All possible states for a d^7 configuration (10 quartet and 40 doublet) were calculated. For the $S = 1$ complexes (**3** and **4**), the CAS(8,6) active space was comprised of eight electrons distributed across the Co 3d shell and one (imino)semiquinonate-based MO (i.e., the SOMO of the ligand radical). Ten quintet and 35 triplet states were included. Dynamic electron correction was incorporated using *N*-electron valence state second-order perturbation theory (NEVPT2).[69] Parameters related to spin-orbit coupling (*g*-values and ZFS) were calculated by applying the effective Hamiltonian method to the multi-configurational CASSCF/NEVPT2 wavefunctions.[70-71] As shown in Tables S4-S6, overall agreement between the experimental and computed parameters was improved by using the

NEVPT2 procedure in tandem with the larger def2-TZVP basis set. Thus, all computed values provided in the main text are derived from CASSCF/NEVPT2 calculations that employed the def2-TZVP basis set. Ligand field energies for the Co 3d orbitals were generated from CASSCF/NEVPT2 calculations using a procedure (*ab initio* ligand field theory, AILFT) developed by Atanasov and coworkers.[6,72] Exchange coupling constants (J) were obtained from DFT calculations (B3LYP functional; def2-TZVP basis set) using the broken symmetry approach (H_{ex} = $-2JS_A \bullet S_B$).[73-74] A geometry-optimized model of the hypothetical complex, $[Co(\mathbf{L^{O,N}})(pz^{Me,Ph})_3]^+$, was generated from DFT calculations that employed the Becke-Perdew (BP86)[75-76] functional and def2-TZVP basis set. Atomic coordinates for this model are provided in Table S9.

III. Results and Discussion

A. Syntheses and X-ray Structures.   The syntheses and X-ray structures of complexes **1** and **3** were reported recently by Kumar and Fiedler.[54]   Complex **2** was prepared by reaction of $[Co(Tp^{Ph2})(OAc)(Hpz^{Ph2})]$ with the sodium salt of 4,6-di-*tert*-butyl-2-aminothiophenolate ($\mathbf{L^{S,N}}$) in CH_2Cl_2.   Similarly, reaction of $[Co(Tp^{Ph2})(OAc)(Hpz^{Ph2})]$ with the monoanion of 3,5-di-*tert*-butylcatechol ($HCat^{tBu2}$) in a CH_2Cl_2/MeOH mixture generated the complex $[Co(Tp^{Ph2})(HCat^{tBu2})]$ (*not isolated*).   In the presence of trace amounts of O_2, the catecholate ligand of this unstable complex oxidizes over several hours to the corresponding semiquinonate ($\mathbf{L^{O,O}_{SQ}}$), thereby giving rise to complex **4**.   Finally, one-electron oxidation of $[Co(Tp^{Ph2})(\mathbf{L^{O,N}_{ISQ}})]$ (**3**) with $AgPF_6$ in CH_2Cl_2 yielded the cationic complex $[\mathbf{5}]^+$, which is paired with a PF_6 counteranion.

Single-crystals of complexes **2**, **4**, and **5** were studied by X-ray diffraction using procedures described in the Experimental Section.   Details of the crystallographic experiments are summarized in Table S1, and relevant metric parameters are provided in Tables S2 and S3.   The X-ray structures confirmed that **1-5** are mononuclear, five-coordinate cobalt complexes consisting of a facially-coordinating Tp^{Ph2} chelate and bidentate $\mathbf{L^{X,Y}}$ ligand, as illustrated in Figure 1 for **2** and **5**.   The average $Co–N_{Tp}$ bond distance varies only slightly across the series, ranging from 2.05 Å (**5**) to 2.13 Å (**2**); these bond distances are characteristic of high-spin, pentacoordinate Co(II) complexes with Tp ligands.[54,77-78]   The coordination geometries are best described as distorted trigonal bipyramidal (tbp), as each complex has a τ-value greater than 0.5.[79]   The position of complexes **1-5** on the continuum between ideal tbp and square pyramidal (spy) geometries was also quantified using the continuous shape method, as implemented in the SHAPE program.[80-81] This analysis found that complexes **1** and **2** lie much closer to the tbp limit, whereas **3-5** are intermediate between tbp and spy (the SHAPE results are reported in Tables S2 and S3).   In all cases there are considerable distortions from ideality.   Specifically, the bond angles in the equatorial planes deviate from the ideal tbp value of 120º by as much as ±25º, largely because the Tp^{Ph2} scaffold constrains the angle between the two equatorial N_{Tp}-donors to ~95º.   As discussed later in the manuscript, this equatorial distortion has substantial consequences for the magnetic properties of **1-5**.
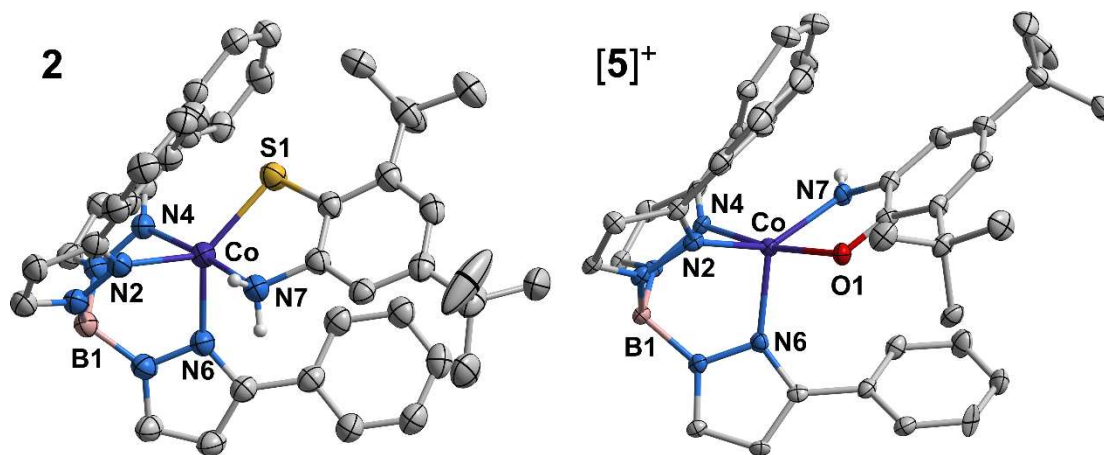
Figure 1. Thermal ellipsoid plots of **2** and **5** (40 and 50% probability, respectively) obtained from X-ray crystal structures. Non-coordinating solvent molecules and most hydrogen atoms have been omitted for clarity, as well as the Ph-rings at the 5-positions of the Tp^{Ph2} ligand. The PF_6^- counteranion in the structure of **5** is not shown.

The amino donors of the $L^{O,N}$ and $L^{S,N}$ ligands occupy an axial position in **1** and **2**, respectively, whereas the (thio)phenolate donors are located in the equatorial plane (Figure 1, left). Interestingly, oxidation of the $L^{O,N}$ ligand to $L^{O,N}_{ISQ}$ (in **3**) or $L^{O,N}_{IBQ}$ (in **5**) reverses the ligand orientation, such that the *O*-atom donor is now axial in the latter two complexes (Figure 1, right). As depicted in Scheme S1, the changes in $L^{O,N}$ oxidation state are evident in the shortening of O–C and N–C bond distances across the **1**→**3**→**5** series, as well as the increasing deviation of C–C bonds from the aromatic value of 1.40 ± 0.02 Å. Following the metrical oxidation state (MOS) method of Brown,[82] the $L^{O,N}_{IBQ}$ ligands of the two independent complexes in the structure of **5** carry charges of +0.07 and +0.17, close to the ideal value of zero for an IBQ ligand (for comparison, the $L^{O,N}_{ISQ}$ ligand of **3** has an MOS of –0.95). Thus, complexes **1, 3**, and **5** constitute a unique redox series in which the cobalt center remains divalent and the $L^{O,N}$ ligand exists in each of its three possible oxidation states. Similarly, the X-ray structure of **4** is fully consistent with a cobalt(II)-semiquinonate radical description,[83] as suggested by the MOS of –1.06 calculated for the $L^{O,O}_{SQ}$ ligand. The structures of **3** and **4** are isomorphous and display very similar metric parameters (Table S3).

B. Magnetic Susceptibility Studies. Solid-state samples of complexes **1-5** were examined with dc magnetometry. Figures 2 and S17 display the measured paramagnetic susceptibility data and fits for complexes **1-5**. The linear dependence of $\chi_P \cdot T$ values above ~50 K in each $\chi_P \cdot T$ vs.

T plot is indicative of substantial temperature-independent paramagnetism (TIP), partially due to field-induced mixing with proximal excited states. This hypothesis is supported by multiconfigurational calculations that reveal the presence of multiple low-lying excited states (*vide infra*). However, we cannot rule out the possibility that other factors, such as Pauli paramagnetism from trace metallic impurities, contribute to the linear increase of $\chi_P \bullet T$ at high temperatures. Thus, the term temperature-independent magnetism (TIM) is employed herein to refer to the sum of these multiple contributions.

Figure 2 (red) displays paramagnetic susceptibility data for **1** between 1.8 K and 275 K. The measured value of $\chi_P \bullet T$ decreases linearly with temperature from 3.41 cm^3 K mol^{-1} at 275 K to 2.71 cm^3 K mol^{-1} at 53 K. Further lowering of temperature results in a precipitous drop of $\chi_P \bullet T$ to 2.01 cm^3 K mol^{-1} at 1.8 K. The linear dependence above ~50 K is due to TIM and the downturn in $\chi_P \bullet T$ below ~50 K is indicative of ZFS. The fact that this drop in $\chi_P \bullet T$ occurs at the relatively high temperature of ~50 K suggests that the ZFS is quite large. Magnetic susceptibility data collected for complex **2**, shown in Figure 2 (green), follow a similar pattern. In this case, the value of $\chi_P \bullet T$ at 275 K, 3.26 cm^3 K mol^{-1}, decreases linearly to 2.79 cm^3 K mol^{-1} at 75 K before markedly dropping to 2.17 cm^3 K mol^{-1} at 1.8 K. The $\chi_P \bullet T$ values of **1** and **2** at 275 K are higher than the spin-only value of 1.875 cm^3 K mol^{-1}, but still within the range of ~2.1–3.4 cm^3 K mol^{-1} reported for strongly anisotropic, high-spin Co(II) ions.[84] The data for complex **5**, shown in Figure S16, also exhibit the same general trend, albeit with lower-than-expected values for $\chi_P \bullet T$ over the entire temperature range. The magnetic susceptibility data collected for **1**, **2**, and **5** were modeled using an $S = 3/2$ spin-Hamiltonian and the fits yielded negative axial ZFS (*D*) values of –41.4(1), 77.7(5), and –29.6(3) cm^{-1} for **1**, **2**, and **5**, respectively. Although it is often difficult to determine the sign of *D* from magnetic susceptibility results, positive *D*-values led to physically unreasonable fits for **1**, **2**, and **5**. The quality of the fits were insensitive to the value of the rhombic ZFS term (*E*) in all three cases.

The magnetometry data indicate that **1** and **2** possess very large and negative magnetic anisotropy; this conclusion is further supported by spectroscopic and computational studies (*vide infra*). The large magnitude of the *D*-values is the result of unquenched orbital angular momentum. In such cases, the spin-Hamiltonian model breaks down and the validity of the ZFS parameters is questionable. Nevertheless, the values extracted from our magnetometry experiments provide useful parameters by which to evaluate results obtained from multiple physical techniques, as well

as a means to compare our findings to those reported in the literature. To this end, Tables S7 and S8 summarize the previously-reported spin-Hamiltonian parameters of numerous five-coordinate Co(II) complexes. These complexes mostly fall into two broad classes that feature either tripodal tetradentate chelate ligands (e.g., TMPA, tren)[85-98] or N_3 pincer[99-106] ligands, although a handful of examples do not belong to either class.[107-109] Interestingly, the D-values of **1** and **2** fall well outside the normal range of $-20 < D < +20$ cm^{-1} observed for Co(II) complexes with tbp geometries. We will discuss below the structural basis for the unusually large and negative anisotropy of these Tp^{Ph2}-containing complexes, which do not belong to either the tripodal or pincer classes of five-coordinate Co(II) complexes.
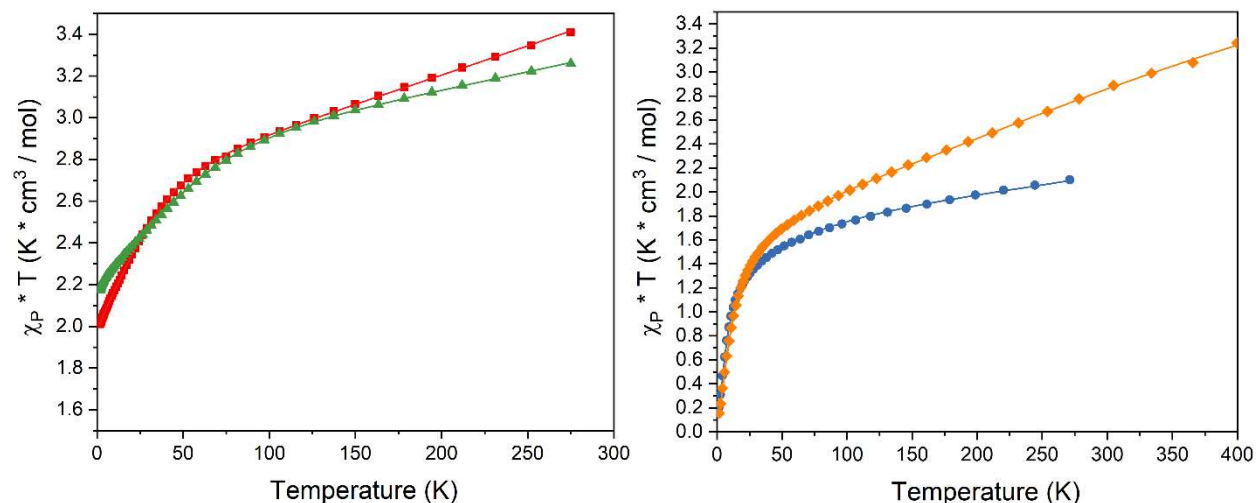

Figure 2. *Left*: Paramagnetic susceptibility for complexes **1** (red squares) and **2** (green triangles) plotted as $\chi_P \cdot T$ vs. T, along with the best fits to the data. The TIM corrections were used as parameters in the fits, as described in the Experimental Section. Fit parameters for **1**: $S = 3/2$, $g_\perp = 2.140(2)$, $g_\parallel = 2.6615(4)$, $D = -41.4(1)$ cm^{-1}, TIM = 0.00300(1) cm^3 mol^{-1}. Fit parameters for **2**: $S = 3/2$, $g_\perp = 2.096(7)$, $g_\parallel = 2.7898(6)$, $D = -77.7(5)$ cm^{-1}, TIM = 0.00201(4) cm^3 mol^{-1}. *Right*: Paramagnetic susceptibility for complexes **3** (blue circles) and **4** (orange squares) plotted as $\chi_P \cdot T$ vs. T, along with the best fits to the data. The TIM correction for **4** was used as a parameter in the fit, as described in the Experimental Section, while a fixed value was used for **3**. Fit parameters for **3**: $S = 1$, $g_\perp = 2.049(6)$, $g_\parallel = 3.176(4)$, $D = -168(3)$ cm^{-1}, $|E| = 8.68(2)$ cm^{-1}, TIM = 0.0017(2) cm^3 mol^{-1} (fixed). Fit parameters for **4**: $S = 1$, $g_\perp = 2.46(2)$, $g_\parallel = 3.003(6)$, $D = -135(5)$ cm^{-1}, $|E| = 11.6(1)$ cm^{-1}, $J = -121(4)$ cm^{-1}, TIM = 0.00132(5) cm^3 mol^{-1}.

Using the Evans method, we previously determined that complex **3** features an $S_{Tot} = 1$ ground state arising from antiferromagnetic (AF) coupling between the high-spin Co(II) center and $\mathbf{L^{O,N}_{ISQ}}$

ligand radical.[54] In this study, paramagnetic susceptibility of solid-state samples of **3** were measured from 1.8 to 271 K; the resulting data and best fit are displayed in Figure 2 (purple). Upon cooling from 271 to 107 K, the value of $\chi_P \cdot T$ decreases quasi-linearly from 2.10 to 1.76 cm^3 K mol^{-1}. At $T < 100$ K, the value of $\chi_P \cdot T$ drops dramatically to 0.21 cm^3 K mol^{-1} at 1.8 K due to large ZFS. Accounting for the TIM correction, the value of $\chi_P \cdot T$ levels off at approximately 1.6 cm^3 K mol^{-1} in the high-temperature regime. No upward deviation in the highest-temperature data points was observed, indicative of little thermal population of the excited $S_{Tot} = 2$ state (measurements at $T > 300$ K revealed sample instability; see Figure S7). This result suggests that the magnitude of the isotropic exchange coupling constant (J) is quite large for **3**, and thus modeling the system with two coupled spins ($S_{Co} = 3/2$ and $S_{ISQ} = 1/2$) was not feasible. Instead, an effective $S = 1$ spin-Hamiltonian model was employed in simultaneous fits of the variable-temperature susceptibility and the reduced magnetization data collected at 2, 4, and 8 K (Figure 3). This procedure yielded the parameters listed in the caption of Figure 2, which correspond to the total $S = 1$ system. To determine the "intrinsic" ZFS parameters of the Co(II) center (D_{Co} and E_{Co}), the $S = 1$ parameters were deconvoluted using equations 1 and 2, which are derived from Clebsch-Gordan spin projection (see the Supporting Information for more details).[110,111] Note that the **g**-tensor of the $\mathbf{L^{O,N}_{ISQ}}$ radical was fixed at 2.00 (there is no ZFS tensor for $\mathbf{L^{O,N}_{ISQ}}$ since $S_{ISQ} = 1/2$). Application of equations 1 and 2 provides the following "local" spin-Hamiltonian parameters for the Co(II) ion: $g_{Co,\perp} = 2.040(6)$, $g_{Co,\parallel} = 2.941(4)$, $D_{Co} = -112(3)$ cm^{-1}, and $|E_{Co}| = 5.79(2)$ cm^{-1}. The remarkably large magnitude of the D_{Co} value is suggestive of spin-orbit coupling involving quasi-degenerate electronic states, as discussed further below.

$$\boldsymbol{D}_{Co} = \tfrac{2}{3}\boldsymbol{D}_{total} \qquad (1)$$

$$\boldsymbol{g}_{Co} = \tfrac{4}{5}\boldsymbol{g}_{total} + \tfrac{1}{5}\boldsymbol{g}_{ISQ} \qquad (2)$$
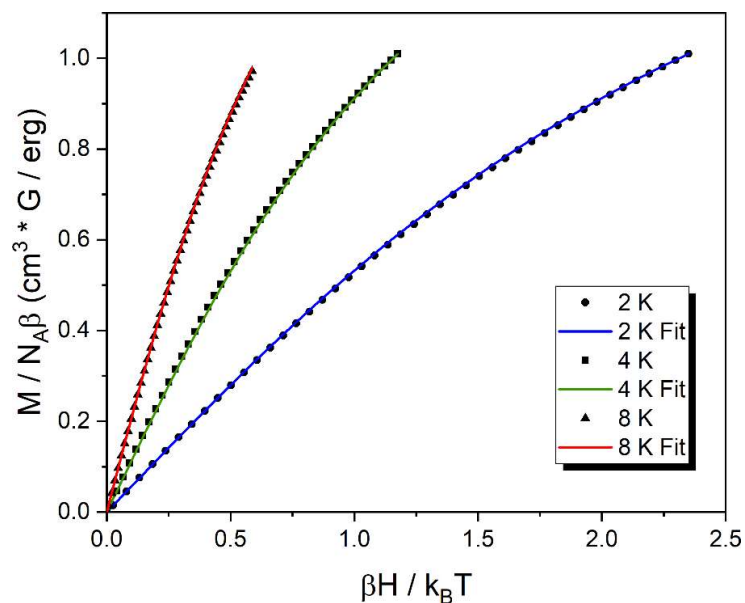
Figure 3. Reduced magnetization data for complex **3** measured at 2, 4, and 8 K. The best fits to the data were generated with the following parameters: $g_\perp = 2.049(6)$, $g_\parallel = 3.176(4)$, $D = -168(3)$ cm^{-1}, and $|E| = 8.68(2)$ cm^{-1}. These parameters were deconvoluted with Clebsch-Gordan spin projection to obtain the "intrinsic" parameters corresponding to the Co(II) center.

　　　Even though modeling the isotropic exchange coupling constant (J) for **3** with two antiferromagnetically coupled spins ($S_{Co} = 3/2$ and $S_{ISQ} = 1/2$) was not feasible, it was possible to utilize the "intrinsic" g-values and ZFS tensor obtained from the Clebsch-Gordan spin projection as fixed parameters in simulations using different values for J to establish an upper limit. The simulations using various values for J are reported in Figure S15. The simulations suggest that $J \leq$ –300 cm^{-1} for **3**, indicative that the antiferromagnetic coupling in this complex is stronger than that in **4** (*vide infra*).

　　　Paramagnetic susceptibility data for the isostructural cobalt(II)-semiquinonate complex (**4**) collected between 1.8 and 400 K are shown in Figure 2 (orange). Like **3**, complex **4** displays a steep drop in $\chi_P \cdot T$ below ~50 K, reaching a value of 0.15 cm^3 K mol^{-1} at 1.8 K. Above ~100 K, the value of $\chi_P \cdot T$ increases approximately linearly from 1.97 to 3.24 cm^3 K mol^{-1} at 400 K. The increase in $\chi_P \cdot T$ over this high-temperature range is attributable to a combination of TIM and partial thermal population of an excited $S_{Tot} = 2$ spin state. Thus, this dataset was modeled with two antiferromagnetically coupled spins, $S_{Co} = 3/2$ and $S_{SQ} = 1/2$, using the Hamiltonian:

$$\hat{H} = \beta(\vec{S}_{Co}\boldsymbol{g}_{Co} + \vec{S}_{SQ}\boldsymbol{g}_{SQ})\vec{H} + \vec{S}_{Co}\boldsymbol{D}_{Co}\vec{S}_{Co} - 2J\vec{S}_{Co}\vec{S}_{SQ}$$

Using this model, a *J*-value of −121(4) cm^{-1} was obtained from fits of the experimental magnetic susceptibility data, along with the spin-Hamiltonian parameters provided in the figure caption. Like **3**, complex **4** features a large and negative *D*-value of −135(6) cm^{-1}. In the next section, we will present spectroscopic data that directly validates the unusually large easy-axis anisotropy observed in magnetic susceptibility studies of **3** and **4**.

Magnetic susceptibility data were also collected for complex **5** and the results are presented in Figure S16-S18. Modeling the data provided g_{ave} and *D*-values of 2.103(6) and −29.6(3) cm^{-1}, respectively. Reduced magnetization data for **5** were also collected and simultaneously fit with the susceptibility data (Figure S19). This fit led to the same parameters as the individual susceptibility fit, but with greater precision (g_{ave} = 2.103(1), *D* = −29.4(1) cm^{-1}). Thus, the results from fitting the susceptibility and reduced magnetization data simultaneously are reported in Table 1. These spin-Hamiltonian parameters should be regarded with caution given that samples of **5** were not analytically pure (see Experimental Section). Nevertheless, the magnetometry data indicate that **5** is a high-spin Co(II) *S* = 3/2 system with less pronounced negative anisotropy than **1** and **2**. These conclusions are supported by FIRMS and HFEPR experiments that yielded more reliable spin-Hamiltonian parameters for **5**.

C. Spectroscopic Studies: FIRMS and HFEPR. FIRMS experiments were performed on *n*-eicosane mulls of all five complexes. Normalized transmission spectra as a function of magnetic field are shown for the three *S* = 3/2 complexes as color plots in Figure 4. Resonance absorptions that change position with increasing magnetic field are highlighted in blue, whereas regions lacking field-dependent features are shown in yellow (the color trend represents the amplitude of the field-induced changes in the transmission spectra). The vertical stripes are artifacts arising from sharp vibrational absorptions, while white regions correspond to spectral ranges without reliable data due the low power of THz radiation in those regions. In complex **1**, we detected a zero-field (zf) resonance of magnetic origin at 84.7 cm^{-1} (Figure 4, left). This feature arises from the $m_S = |\pm 3/2\rangle \rightarrow |\pm 1/2\rangle$ transition, which has an energy of $\Delta = 2(D^2 + 3E^2)^{1/2}$ for an *S* = 3/2 system. It is not possible to derive *D* and *E* from a zf experiment on a Kramers system like Co(II), thus HFEPR experiments were also performed on the same sample in the frequency range of 50 – 500 GHz. Figure 5 (top) shows a textbook-quality HFEPR spectrum of complex **1** measured at 10 K and 140 GHz, accompanied by its simulation assuming a random distribution of crystallites. All the peaks are turning points of the intra-Kramers transition within the $m_S = |\pm 3/2\rangle$ doublet,

confirming the negative *D*-value of **1**. The final spin Hamiltonian parameters for complex **1** were obtained from the combined FIRMS/HFEPR field vs. energy (or frequency) map shown in Figure 4 (left), and the results are summarized in Table 1.
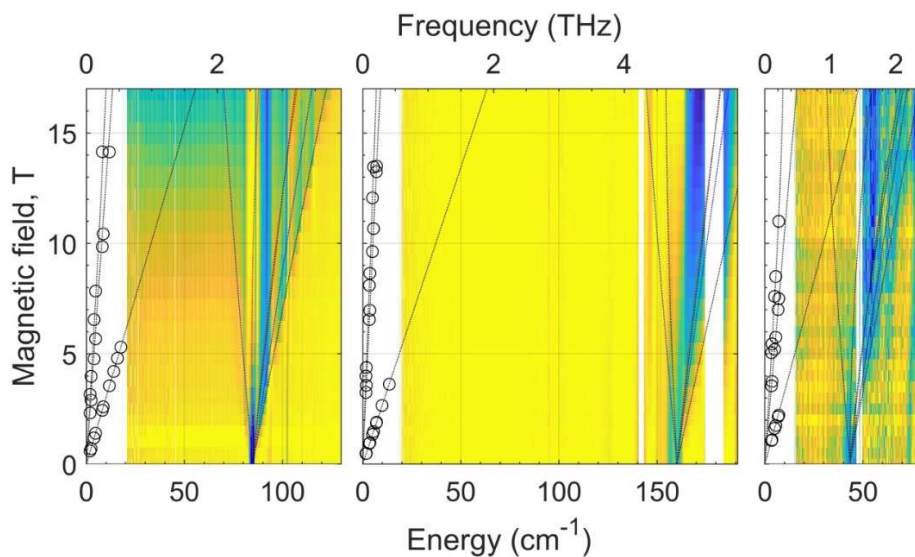

Figure 4.   Color maps (Intensity vs. field and energy/frequency) of far-infrared resonance absorption measured for complexes **1** (left), **2** (middle), and **5** (right) at 4.6 K. Regions of magnetic absorption are indicated with blue. The lines are simulations of turning points in the powder spectra that assume the (best-fitted) spin Hamiltonian parameters shown in Table 1. The circles at low frequencies (below those accessible by FIRMS) correspond to the observed HFEPR resonances.

FIRMS data measured for **2** (Figure 4, middle) are partially affected by artifacts, but the inter-Kramers transition is clearly evident at 161.2 cm^{-1} in zero field. Complex **2** produced almost the same quality of HFEPR spectra as **1**, one of which is shown in Figure 5 (middle) as recorded at 10 K and 101 GHz, together with its simulation. The final spin Hamiltonian parameters for complex **2** were obtained from the combined FIRMS/HFEPR field vs. energy (or frequency) map via least-square fit as shown in Figure 4 (middle), and the results are summarized in Table 1. The *D*-value of –77.4 cm^{-1} measured for **2** is consistent with the sizable increase in magnetic anisotropy from **1→2** observed by magnetometry (*vide supra*).
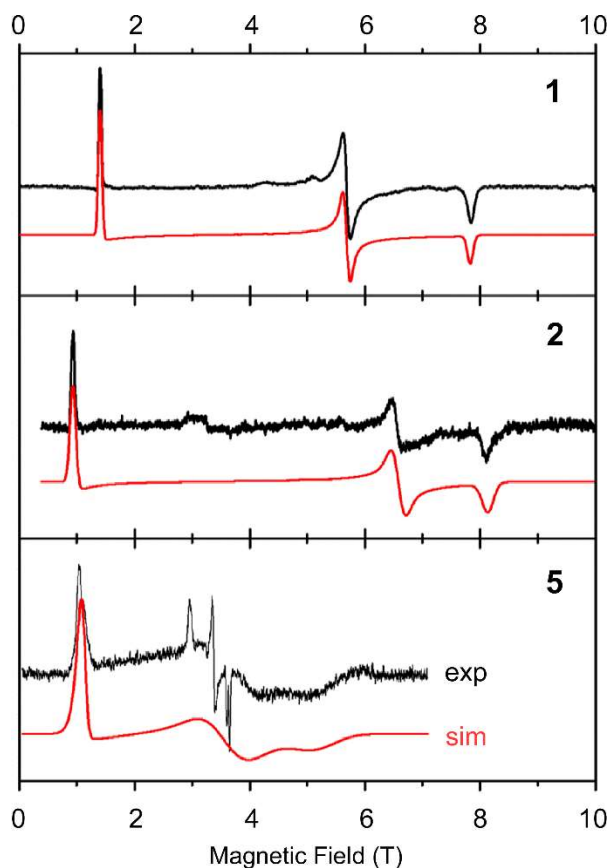
Figure 5. HFEPR spectra of the three $S = 3/2$ complexes (black traces) at 10 K and varying frequency. The simulated spectra (red traces) assume a random distribution of crystallites. The spin-Hamiltonian parameters listed here are derived from the simulation that provided the best agreement with experiment at the indicated frequency. Complex **1**: frequency: 140.1 GHz, $D = -38.7$ cm^{-1}, $E = -10.0$ cm^{-1} ($E/D = 0.26$), $g_x = 2.20$, $g_y = 2.08$, $g_z = 2.51$; complex **2**: frequency: 101.3 GHz, $D = -77.4$ cm^{-1}, $E = -11.8$ cm^{-1} ($E/D = 0.15$), $g_x = 2.31$, $g_y = 2.20$, $g_z = 2.62$; complex **5**: frequency: 101.4 GHz, $D = -18.8$ cm^{-1}, $E = -6.3$ cm^{-1} ($E/D = 0.33$), $g_x = 2.05$, $g_y = 2.0$, $g_z = 2.4$. The three sharp resonances [$g = 2.0, 2.15, 2.45$] are interpreted as the powder pattern of a low-spin ($S = 1/2$) Co(II) impurity[112] and are not simulated.

Complexes **3** and **4** are EPR-silent even at the highest frequencies available to us, indicative of a very large absolute value of D. A single zf resonance of magnetic origin was observed by FIRMS at 117.5 and 130.0 cm^{-1} for **3** and **4**, respectively (Figure 6). Given the negative sign of D, as suggested by magnetometry and calculations, this feature corresponds to the $|D + E|$ transition, where it is assumed that D and E have the same sign. The fact that a second zf resonance, corresponding to the $|D - E|$ transition, is not observed by FIRMS is consistent with the negative anisotropy of these complexes and indicates a sizable magnitude of E, which makes the next higher-energy spin sublevel $m_S = |+1\rangle$ unpopulated at low temperature. The $\Delta m_S = \pm 2$ transition

between the $m_S = |-1\rangle$ and $|+1\rangle$ levels is not observed for either **3** or **4** either, which suggests that the *E*-values are smaller than half of the lower boundary of the FIRMS transmittance window (~20 cm^{-1}). Thus, based on the FIRMS data, we can conclude that the *D*-values of **3** and **4** fall within the range of −100 to −130 cm^{-1}, in excellent agreement with the magnetometry results.[113,114-115]

FIRMS spectra of complex **5** showed a rather weak inter-Kramers resonance at 46 cm^{-1} in zero field (Figure 4, right). The HFEPR response (Figure 5, bottom) was problematic. Although the low-field signal at 1 T at 101 GHz can be clearly identified as the parallel turning point of the intra-Kramers transition within the $m_S = |\pm 3/2\rangle$ doublet, analogously to complexes **1** and **2**. The group of three sharp resonances at higher field (3−4 T) cannot be reconciled with an $S = 3/2$ system, and must represent a different spin species. We tentatively identify those signals as originating from a low-spin ($S = 1/2$) Co(II) impurity characterized by a rhombic *g*-tensor. One can also, however, recognize two much broader underlining lines that we interpret as the two perpendicular turning points of the intra-Kramers transition within the $m_S = |\pm 3/2\rangle$ doublet. The final spin Hamiltonian parameters for complex **5** were obtained from the combined FIRMS/HFEPR map as shown in Figure 4 (right), and the results are summarized in Table 1. Unlike complexes **1** and **2**, we did not perform a least-square fit due to uncertainties arising from the broadness of the resonance positions; hence, we refrained from estimating the errors for the parameters.
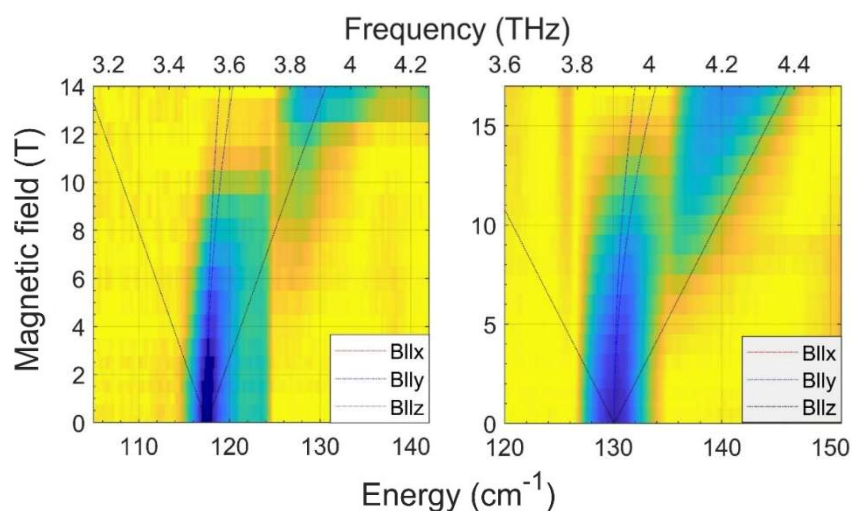

Figure 6.   Color maps (Intensity vs. field and energy/frequency) of far-infrared resonance absorption measured for complexes **3** (left) and **4** (right) at 4.6 K. Regions of magnetic absorption are indicated with blue in the colored FIRMS maps. The lines are simulations of turning points in the powder spectra that assume the spin-Hamiltonian parameters shown in Table 1.

D. Theoretical Calculations

    D.1. Quantum chemical calculations of $[Co^{II}(Tp^{Ph2})(L^{O,N})]$ (1) and $[Co^{II}(Tp^{Ph2})(L^{S,N})]$ (2).
The magnetic susceptibility, HFEPR, and FIRMS experiments described in previous sections revealed that both **1** and **2** possess sizable ZFS, as indicated by the results summarized in Table 1. The large and negative magnetic anisotropy exhibited by **1** and **2** is unusual for five-coordinate Co(II) complexes, especially those with tbp geometry (*vide supra*). We have applied quantum chemical theory to truncated models of **1** and **2** with the goal of understanding the structural origins of their atypical magnetic parameters. Ligand-field (LF) energies, *g*-values, and ZFS parameters were computed using the complete active-space self-consistent field (CASSCF) approach, as implemented in ORCA 4.0. The active space consisted of the 7 d-electrons in the Co(3d) shell (i.e., CAS(7,5)). These calculations computed energies for all quartet and doublet ligand-field states of the Co(II) center. The CASSCF method was supplemented with *n*-electron valence second-order perturbation theory (NEVPT2), which substantially improves agreement between the experimental and computed spin-Hamiltonian parameters (Tables S4-S6). Additional details are provided in the Computational Methods section.

    As shown in Table 1, our CASSCF/NEVPT2 calculations reproduce the negative magnetic anisotropy of **1** and **2**, and the computed *E/D* ratios and *g*-values are also consistent with the experimental data. The splitting of the $S = 3/2$ ground state into $m_S = \pm 1/2$ and $\pm 3/2$ doublets is due to mixing between the ground and excited states induced by spin-orbit coupling (SOC). From the CASSCF/NEVPT2 calculations, it is possible to quantify the impact of each excited state on the molecular *D*- and *E*-values; these results are summarized in Figure 7 for **1** and **2**. In both cases, ZFS arises almost entirely from contributions of the four lowest-energy quartet excited states, which belong to either A′ or A″ representations in C_s symmetry. The net effect of the doublet states on ZFS is comparatively minor. The dominant contributor to the negative sign of *D* is the lowest-energy excited state, $^4A′(1)$, which is predicted to lie only 1527 and 834 cm^{-1} above the $^4A″(1)$ ground state for **1** and **2**, respectively. Smaller positive contributions from the higher-energy $^4A″(2)$ and $^4A″(3)$ states are offset by the negative contribution of the second A′ excited state, $^4A′(2)$. However, the two $^4A″$ excited states are responsible for the observed rhombicity of **1** and **2**, as they make the largest contributions to the *E* parameter.

Table 1. Experimental and Theoretical spin-Hamiltonian Parameters for Complexes **1–5**. [a]

complex (spin)	g-values			ZFS parameters			J (cm^{-1}) [c]	method(s)
	g_1	g_2	g_3	D (cm^{-1})	E (cm^{-1})[b]	$|E/D|$		
1	2.08(2)	2.20(3)	2.51(1)	−38.7(1)	−10.0(1)	0.26	NA	FIRMS/HFEPR
($S = 3/2$)	2.140(2)	2.140(9)	2.6615(4)	−41.4(1)	ND	ND	NA	mag. suscept.
	2.012	2.227	2.636	−49.4	−13.2	0.27	NA	QCT [e]
2	2.216(6)	2.326(6)	2.72(1)	−77.4(2)	−11.8(3)	0.15	NA	FIRMS/HFEPR
($S = 3/2$)	2.096(7)	2.096(7)	2.7898(6)	−77.7(5)	ND	ND	NA	mag. suscept.
	1.954	2.186	2.842	−70.1	−14.7	0.21	NA	QCT [e]
3	g_{iso} = 2.00 [d]			$|D + E|$ = 117.5 cm^{-1}			ND	FIRMS
($S = 1$)	2.040(6)	2.040(6)	2.941(4)	−112(3)	−5.79(2)	0.052	≤ −300	mag. suscept.
	1.903	2.030	3.402	−170.6	−8.2	0.048	−330	QCT [e]
4	g_{iso} = 2.00 [d]			$|D + E|$ = 130 cm^{-1}			ND	FIRMS
($S = 1$)	2.46(2)	2.46(2)	3.003(6)	−135(6)	−11.6(1)	0.086	−121(4)	mag. suscept.
	1.881	2.028	3.436	−178.8	−12.1	0.068	−128	QCT [e]
5	2.00	2.05	2.40	−18.8	−6.26	0.33	NA	FIRMS/HFEPR
($S = 3/2$)	2.003(4)	2.003(4)	2.304(1)	−29.6(3)	ND	ND	NA	mag. suscept.
	2.143	2.267	2.437	−21.2	−5.9	0.28	NA	QCT [e,f]

[a] NA = not applicable; ND = not determined. [b] The sign of E obtained by HFEPR and magnetic susceptibility is arbitrarily assumed to be the same as that of D. [c] J-values were computed using the $H_{ex} = -2J \cdot S_A \cdot S_B$ formalism. [d] Because FIRMS simulations are largely insensitive to g-values, an isotropic **g**-tensor (g_{iso} = 2.00) was employed. [e] QCT = parameters derived from quantum chemical calculations employing the CASSCF/NEVPT2 approach (def2-TZVP basis set). [f] QCT values were computed for structure B in the X-ray structure of **5** (see Table S6).
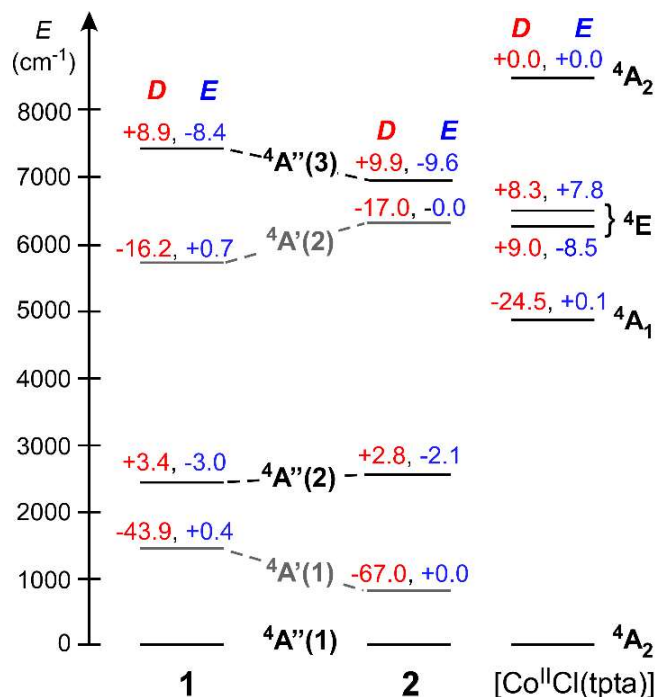
Figure 7. CASSCF/NEVPT2 computed energies of the five lowest-energy quartet states of complexes **1**, **2**, and [Co^{II}Cl(tpta)]$^+$. The contribution of each excited state to the molecular *D*- and *E*-parameters is indicated in red and blue, respectively.

Based on insights provided by the CASSCF/NEVPT2 calculations, we are now able to rationalize the much greater negative anisotropy of **1** and **2** compared to 5C Co(II) complexes with tripodal ligands, such as TMPA and Me$_6$tren. Figure 7 compares the LF energies of **1** and **2** to those computed for [Co^{II}Cl(tpta)]$^+$, where tpta is the tetradentate chelate tris[(1-phenyl-1*H*-1,2,3-tris(triazol-4-yl)methyl]amine. The latter complex was the subject of a recent experimental study that found the following spin-Hamiltonian parameters: $g_{1,2,3}$ = 2.22, 2.32, 2.42; D = –9.02 cm^{-1}; $|E|$ = 1.64 cm^{-1}.[88] The three equatorial N–Co–N angles of [Co^{II}Cl(tpta)]$^+$ are roughly equivalent at 112°, resulting in C_{3v} symmetry. The ^{4}A$_2$ ground state is accompanied by four low-lying quartet excited states: ^{4}A$_1$, ^{4}E, and ^{4}A$_2$ in order of increasing energy. These four excited states are largely derived from the $(e)^3(e)^3(a_1)^1$ configuration. From the experimental absorption spectra,[88] it was determined that the ^{4}A$_1$ state of [Co^{II}Cl(tpta)]$^+$ lies 5300 cm^{-1} above the ground state (slightly higher than the computed energy of 4800 cm^{-1}). Like the ^{4}A′(1) state in complexes **1** and **2**, the contribution of the ^{4}A$_1$ state to the *D*-tensor of [Co^{II}Cl(tpta)]$^+$ is negative (–24.5 cm^{-1}). However, this effect is partially offset by the positive contribution of the ^{4}E state (+17.3 cm^{-1}), resulting in an overall computed *D*-value of –6.7 cm^{-1}.
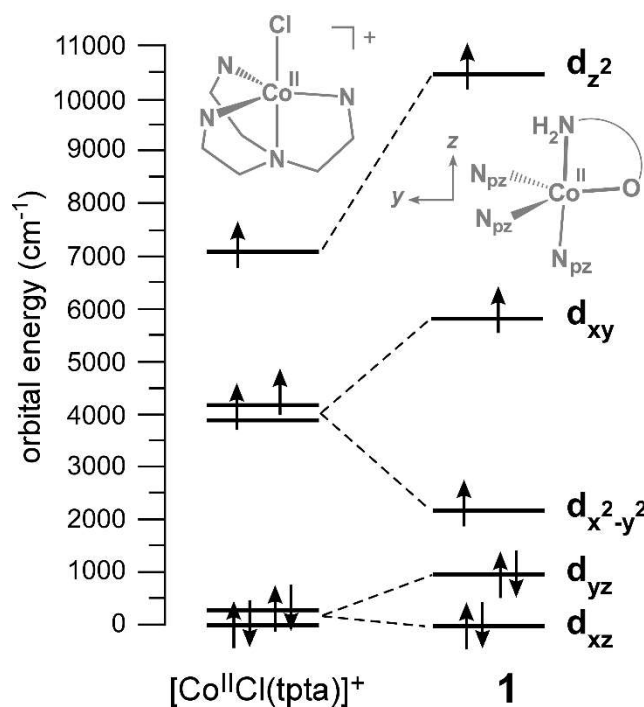
Figure 8. Energy level diagram for the cobalt 3d orbitals of $[Co^{II}Cl(tpta)]^+$ and **1**. Orbital energies were obtained by application of ligand field theory to the NEVPT2 transition energies, as described in Schweinfurth *et al.*[84] The 3d orbitals of **1** are labeled according to their dominant component (the coordinate scheme employed for **1** is indicated in the figure).

Although complexes **1**, **2**, and $[Co^{II}Cl(tpta)]^+$ share tbp geometries, the structural distortions introduced by the facially-coordinating Tp^{Ph2} ligand cause dramatic shifts in ligand-field energies that impact magnetic anisotropy. As noted above, the Tp^{Ph2} ligand of **1** and **2** enforces a ~95° angle between the equatorial pyrazole donors, thereby increasing the equatorial N_{Tp}–Co–O/S angles to around 130° (*vide supra*). The disparity in equatorial bond angles splits the pair of Co $3d_{xy}$- and $3d_{x2-y2}$-based molecular orbitals (MOs) of **1** by 3645 cm^{-1}, as illustrated in Figure 8.[116] The stabilization of the d_{x2-y2} orbital in **1** and **2** accounts for the low energies of the $^4A'(1)$ and $^4A''(2)$ excited states, as these states are generated by one-electron d_{xz}/d_{yz}→d_{x2-y2} excitations. Following perturbation theory, the lower relative energy of the $^4A'(1)$ excited state sharply increases its negative contribution to the magnetic anisotropy. At the same time, the positive contributions of the ^4E state in C_{3v} symmetry are diminished by its splitting into A'/A'' states in C_s symmetry. Thus, the sizable negative *D*- and non-zero *E*-values of **1** and **2** are achieved by removing the C_{3v} symmetry of five-coordinate Co(II) complexes with tripodal ligands.

To further examine this hypothesis, we generated a computational model in which the tridentate Tp^{Ph2} ligand of **1** was "descorpionated" by replacement with three unconstrained, monodentate 1-methyl-3-phenylpyrazole ($pz^{Me,Ph}$) ligands, i.e., $[Co(\mathbf{L^{O,N}})(pz^{Me,Ph})_3]^+$. The structure of $[Co(\mathbf{L^{O,N}})(pz^{Me,Ph})_3]^+$ obtained by DFT geometry optimization features equatorial N–Co–N/O bonds angles of 114°, 117°, and 124°, which are much closer to the ideal value of 120° than those observed in the X-ray structure of **1**. Most notably, the change in molecular geometry from $\mathbf{1}\rightarrow[Co(\mathbf{L^{O,N}})(pz^{Me,Ph})_3]^+$ is accompanied by a dramatic reduction in the magnitude of the computed D-value from −49 to −20 cm^{-1}. Collectively, these results support our thesis that the unusually large and negative D-values of **1** and **2** originate from structural constraints imposed by the scorpionate Tp^{Ph2} ligand.

D.2. Quantum chemical calculations of $[\mathbf{Co^{II}}(^{Ph2}\mathbf{Tp})(\mathbf{L^{O,N}}_{ISQ})]$ (3) and $[\mathbf{Co^{II}}(^{Ph2}\mathbf{Tp})(\mathbf{L^{O,O}}_{SQ})]$ (4). The broken symmetry (BS) approach[73-74] was applied to DFT calculations of **3** and **4** in order to probe cobalt-ligand exchange interactions. These calculations yielded J-values of −529 and −199 cm^{-1} for **3** and **4**, respectively (the $H_{ex} = -2J\cdot S_A S_B$ formalism and Yamaguchi method[117-118] were employed). Thus, DFT correctly predicts that **3** and **4** possess $S = 1$ ground states arising from antiferromagnetic (AF) coupling between the high-spin Co(II) center and the (imino)semiquinonate radical. Furthermore, in agreement with the magnetic susceptibility data, the AF interaction is calculated to be much stronger in **3** than **4**, although BS-DFT overestimates the magnitude of J by ~50 cm^{-1} in the case of **4**. Exchange coupling parameters were also obtained from CASSCF/NEVPT2 calculations, where the active space consisted of 7 d-electrons in the Co(3d) shell and an unpaired electron in an (imino)semiquinonate-based MO (i.e., CAS(8,6)). This approach yielded a J-value of −128 cm^{-1} for **4** – remarkably close to the experimental value of −121(4) cm^{-1} (Table 1). Additionally, this approach gave a J-value of −330 cm^{-1} for **3**, near the upper limit of −300 cm^{-1} established by susceptibility data simulations. In both complexes, the AF exchange is mediated by overlap between the singly-occupied MO (SOMO) of the ligand radical and the $3d_{xy}$-based MO of cobalt, as illustrated in Figure 9. The degree of orbital overlap (S), as computed by BS-DFT, is greater for **3** ($S = 0.39$) than **4** ($S = 0.28$), which accounts for the observed difference in J-values. Spin-density plots for **3** and **4** are shown in Figure S20.
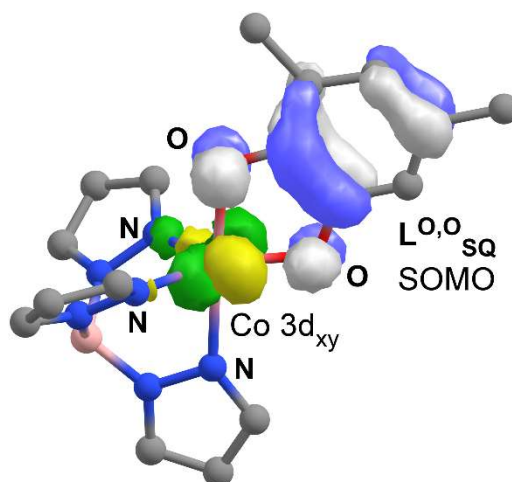
Figure 9. DFT-generated contour plots of the spin-up Co $3d_{xy}$-based MO (green and yellow) and spin-down $L^{O,O}_{SQ}$ π^*-based MO (blue and grey) of complex **4**. These two singly-occupied MOs mediate AF exchange interactions between the Co(II) center and $L^{O,O}_{SQ}$ radical. The phenyl rings of the pyrazole donors have been removed for the sake of clarity.

The CASSCF/NEVPT2 calculations also provide insights into the role of the ligand-based radical in modulating the energies of ligand-field states and, hence, the ZFS parameters. A high-spin Co(II) center possesses 10 quartet LF states, each of which couples to the doublet $L^{O,N}_{ISQ}$ or $L^{O,O}_{SQ}$ radical to generate a pair of quintet (spins "up-up") and triplet (spins "up-down") states. From the relative energies of quintet/triplet pairs arising from the same electronic configuration, it is possible to derive the LF energies of a hypothetical "uncoupled" complex that lacks AF exchange. The results of this procedure are shown in Figure 10 for complex **3**. In the absence of exchange coupling, the computed energy difference between the ground state and first excited state is 793 cm^{-1} (this energy gap is labeled ΔE_1^{UC} in Figure 10; UC = uncoupled). Comparison of the computed LF energies **1** and **3** suggests that oxidation of the $L^{O,N}$ ligand to $L^{O,N}_{ISQ}$ reduces the relative energy of the first excited state by ~700 cm^{-1}, largely by stabilizing the Co $3d_{x2-y2}$ orbital. Thus, changes in ligand oxidation state have a major impact on LF energies, independent of exchange interactions.
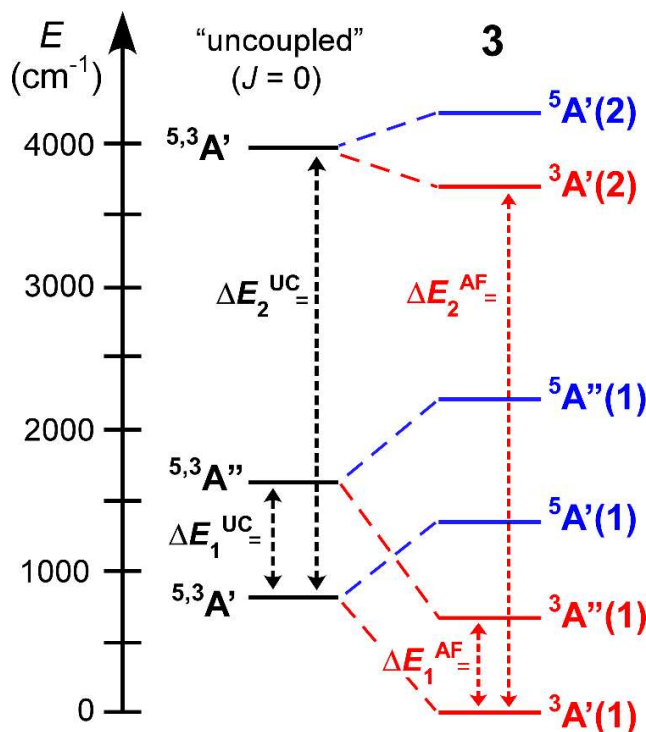
Figure 10. *Right*: CASSCF/NEVPT2 computed energies of the six lowest-energy states of complex **3**. Energy splittings between the three triplet states are indicated by ΔE_1^{AF} and ΔE_2^{AF} (AF = antiferromagnetic). *Left*: Relative energies of ligand-field states in the absence of exchange coupling between Co(II) and $\mathbf{L^{O,N}_{ISQ}}$ (*i.e.*, *J*-value of zero). The energy of each uncoupled (UC) state was calculated by taking the weighted average of the corresponding quintet and triplet energies: $E^{UC} = 3/8\ E(\text{triplet}) + 5/8\ E(\text{quintet})$.

In the presence of AF exchange, the lowest-energy excited state, $^{3}A''(1)$, lies only 650 cm^{-1} above the $^{3}A'(1)$ ground state (ΔE_1^{AF} in Figure 10). This result suggests that coupling to the $\mathbf{L^{O,N}_{ISQ}}$ radical further shrinks the ΔE_1 gap by ~140 cm^{-1}. In contrast, exchange interactions increase the relative energy of the $^{3}A'(2)$ excited state (i.e., $\Delta E_2^{AF} > \Delta E_2^{UC}$), demonstrating that the impact of AF coupling is not uniform across the LF states. In this manner, exchange interactions contribute to the overall magnetic anisotropy. CASSCF/NEVPT2 calculations of complex **4** give rise to a similar pattern of LF states, as evident by the energy-level diagram shown in Figure S21. In this case, the computed ΔE_1^{AF} value is slightly smaller at 505 cm^{-1}.

Inclusion of SOC effects in CASSCF/NEVPT2 calculations of **3** and **4** causes extensive mixing between the $^{3}A'(1)$ ground state and low-lying $^{3}A''(1)$ excited state due to their close proximity. As shown in Figure 11 for **3**, the presence of SOC gives rise to six low-energy states within 1000 cm^{-1}. The two lowest-energy states are separated by only 17 cm^{-1} (δ_1 in Figure 11), while a third

lies at 188 cm^{-1} above the ground-state (δ_2). Calculations of complex **4** provided similar δ_1- and δ_2-values of 26 and 226 cm^{-1}, respectively. These computational results provide a helpful framework for interpreting the experimental magnetic and spectroscopic data presented above. Specifically, we can now assign the zero-field transition observed at 117 and 130 cm^{-1} in FIRMS spectra of **3** and **4**, respectively, to the δ_2 splitting in Figure 11. The CASSCF/NEVPT2 calculations overestimate the size of the zero-field transition by ~50% but correctly predict the modest increase in δ_2 from **3** to **4**.

As noted previously, the ZFS model must be applied cautiously to complexes like **3** and **4** with low-lying LF states. Nevertheless, to a rough approximation, the three lowest-energy states correspond to the $|S, m_S\rangle = |1, \pm 1\rangle$ and $|S, m_S\rangle = |1, 0\rangle$ components of a classical $S = 1$ system with $D < 0$. Following this assumption yields the ZFS parameters reported in Table 1. The computed D-values are larger in magnitude than those extracted from the magnetic susceptibility data, suggesting that the energy of the lowest excited state is underestimated (i.e., the computed values of $\Delta E_1{}^{AF}$ are too low). Despite this, the CASSCF/NEVPT2 results are fully consistent with the large and negative anisotropy observed experimentally for **3** and **4**.
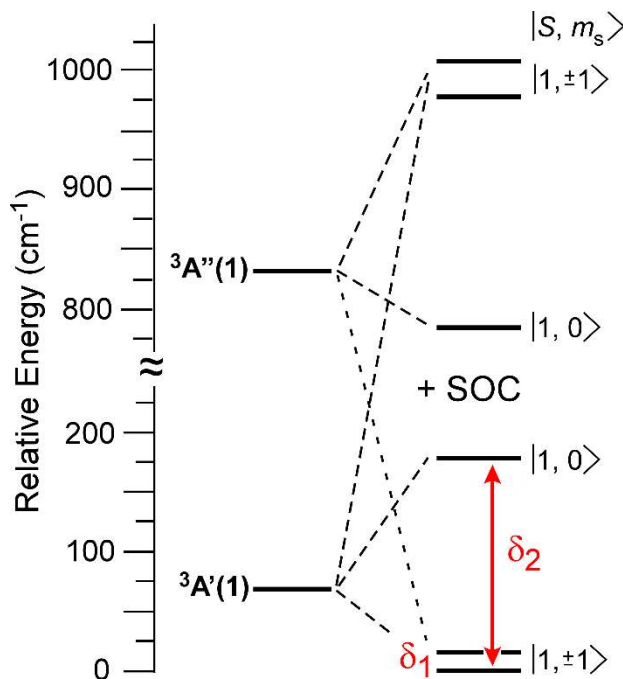

Figure 11. Energy-level diagram illustrating the zero-field splitting of the ^{3}A′(1) ground state and ^{3}A″(1) excited state of **3** due to SOC. Relative energies were obtained by applying the effective Hamiltonian approach to the CASSCF/NEVPT2 wavefunction.

D.3. Quantum chemical calculations of [Co^{II}(^{Ph2}Tp)(L$^{O,N}_{IBQ}$)] [5]$^{+}$. FIRMS and HFEPR studies of complex **5** revealed a strongly rhombic **D**-tensor (E/D = 0.33) and an inter-Kramers splitting of Δ = 46 cm^{-1}, roughly half the magnitude of the Δ-value measured for **1**. The X-ray crystal structure of **5** features two symmetry-independent Co(II) complexes (labeled **5-A** and **5-B**) in the unit cell. The geometries of **5-A** and **5-B** are quite similar and each lies nearly halfway between the spy and tbp limits. CASSCF/NEVPT2 methods were applied to both structures. As summarized in Table S6, the **5-B** structure yields computed D- and E-values (−21 and −5.9 cm^{-1}, respectively) in excellent agreement with the experimental values of D = −18.8 and E = −6.26 cm^{-1} obtained by HFEPR and D = −29.6 cm^{-1} obtained by dc magnetic susceptibility. However, the D-value of −57.4 cm^{-1} calculated for **5-A** is considerably more negative. These results suggest that minor changes molecular geometry can have a major impact on ZFS parameters.

The smaller magnetic anisotropy of **5** can be attributed to the arrangement of its three pseudoequatorial N-donor ligands (N2, N4, and N6 in Figure 1, right). As described above, **1** and **2** exhibit idealized C_s symmetry with equatorial bond angles near 95°, 130°, and 130° (Table S2). In contrast, the three equatorial angles of **5-B** display quite different values of 96.6°, 118.9 °, and 138.6 ° (similar angles are observed for **5-A**; see Table S3). The loss of mirror-plane symmetry causes extensive mixing among the d$_{xz}$/d$_{yz}$ and d$_{xy}$/d$_{x2-y2}$ orbitals, which increases the rhombicity of the molecular **D**-tensor. Although the energy of the first excited state remains rather low at 2130 cm^{-1} for **5-B**, the magnitude of its contribution to axial ZFS is sharply reduced. Thus, for this series of Co(II) complexes, it appears that negative magnetic anisotropy is diminished by loss of any molecular symmetry (in this case the mirror plane).

IV. Conclusions

The development of inexpensive magnetic materials requires the ability to finely tune the spin-states and magnetic anisotropy of transition-metal complexes through ligand design and modification. In this study, we have examined the geometric structures, magnetic properties, and spectroscopic features of a series of pentacoordinate Co(II) complexes (**1-5**; Scheme 1) prepared with redox-active ligands in multiple oxidation states. X-ray crystallographic analysis showed that each complex consists of a high-spin Co(II) center in a distorted tbp coordination geometry formed by the bidentate **L^{X,Y}** and facially-coordinating Tp^{Ph2} ligands. Magnetic susceptibility studies determined that the S = 3/2 ground-states of **1** and **2** possess negative (easy-axis) anisotropy. The

axial ZFS term (D) is sensitive to subtle changes in ligand structure, as evident by the two-fold increase in magnitude when the phenolate O-donor of **1** is replaced with the thiophenolate S-donor of **2** (Table 1). The two complexes with o-(imino)semiquinonate ligands (**3** and **4**) feature $S = 1$ ground states due to antiferromagnetic cobalt-radical exchange interactions.   Magnetic susceptibility experiments of **4** indicate that the $S = 2$ excited state is partially occupied at elevated temperatures and data fitting yielded an exchange coupling constant of $J = -121$ cm^{-1} ($-2J$ formalism). Although it was not possible to exactly quantify the J-value of **3**, the upper limit was established at -300 cm^{-1}, indicating that cobalt-radical exchange interactions are considerably stronger for **3** than **4**.

By taking advantage of recent advances in far-infrared magnetic spectroscopy (FIRMS), we were able to directly measure the zero-field splittings of complexes **1-5**. FIRMS data of the three $S = 3/2$ complexes (**1**, **2**, and **5**) reveal a single magnetic absorption that arises from the inter-Kramers transition, $m_S = |\pm 3/2\rangle \rightarrow |\pm 1/2\rangle = \Delta$. The Δ-values of 84.7 and 161.2 cm^{-1} measured at zero field for **1** and **2**, respectively, are consistent with the large D-values extracted from the magnetic susceptibility data. Parallel HFEPR studies of **1**, **2**, and **5** yielded complete sets of spin-Hamiltonian parameters, which are listed in Table 1. These results demonstrate that two-electron oxidation of the ligand (from $\mathbf{L^{O,N}}$ to $\mathbf{L^{O,N}_{IBQ}}$) is accompanied by a decrease in axial anisotropy and an increase in rhombicity (E/D ratio). In addition, the use of FIRMS proved critical in measuring the ZFS of the two $S = 1$ complexes, which are EPR-silent even at high frequencies. Complexes **3** and **4** each exhibit a single absorption at 117.5 and 130 cm^{-1}, respectively, that corresponds to the $|D + E|$ transition of a $S = 1$ system. While it was not possible to deconvolute the axial and rhombic ZFS terms (a difficulty inherent to triplets with large rhombicity), the collective results indicate that the D-values of **3** and **4** lie between -100 and -130 cm^{-1}. To the best of our knowledge, this study represents the first application of FIRMS to transition-metal complexes with ligand-based radicals.[119,120-121] The anisotropies of **1** and **2** are considerably larger and more negative than those previously reported for five-coordinate Co(II) complexes (Tables S7 and S8), as well as those reported for related four-coordinate Co(II)–X complexes supported by Tp ligands (X = Cl$^-$, NCS$^-$, NCO$^-$, N$_3$$^-$).[122]   Based on quantum chemical calculations that employed the multiconfigurational CASSCF/NEVPT2 approach, we ascertained that the sizable D-values of **1** and **2** are due to deviations in the equatorial bond angles from the ideal value of 120°. Specifically, the Tp^{Ph2} scaffold constrains the equatorial N$_{Tp}$–Co–N$_{Tp}$ bond angle to ~95°,

which stabilizes the lowest-energy singly-occupied Co 3d orbital (i.e., the d_{x2-y2} orbital in Figure 8). The energy gap between the ground state and lowest-energy excited state is reduced as a consequence (Figure 7), triggering an increase in the inter-Kramers splitting due to SOC. The equatorial distortions are also responsible for the rhombic nature of the spin-Hamiltonian parameters measured for **1**. These conclusions are consistent with previous studies by Mallah and coworkers, which found that the anisotropies of pentacoordinate Co(II) complexes with tripodal ligands become more negative and rhombic as the equatorial bond angles deviate from 120°.[91-92] While the large and negative anisotropies of **1** and **2** are promising from the standpoint of SMM design, the rhombic nature of their **D**-tensors is likely to diminish performance. Thus, for Co(II) complexes with tbp geometries, there appears to be a tradeoff between the magnitude of D and rhombicity. Future efforts in our labs will seek to minimize the E-values of Tp-based Co(II) complexes while maintaining the large, negative D-values.

The sizable ZFS observed for the $S = 1$ complexes (**3** and **4**) arises from a similar set of electronic and structural factors. However, in these cases, the anisotropy is further enhanced by exchange coupling between the Co(II) ion and o-(imino)semiquinonate radical. As illustrated in Figure 10, these interactions perturb the relative energies of the ligand-field states, further diminishing the energy gap the ground and first excited states. The high degree of SOC-induced mixing between these two triplet states gives rise to the large and negative anisotropies of **3** and **4**. Thus, the use of redox-active ligands offers another means for chemists to modulate the spin-states and ZFS of transition-metal complexes of relevance to magnetic materials.

Supporting Information

Single-crystal X-ray diffraction parameters (Table S1), bond distances and angles for complexes **1-5** (Tables S2 and S3), computed spin-Hamiltonian parameters (Tables S4-S6), *g*-values and ZFS parameters of previously-reported pentacoordinate Co(II) complexes (Tables S7 and S8), computed structure of $[Co(\mathbf{L^{O,N}})(pz^{Me,Ph})_3]^+$ (Table S9), fits and analysis of magnetic susceptibility data (Figures S1-S19), and crystallographic data in CIF format. This material is available free of charge at http://pubs.acs.org/.

References

1. Krzystek, J.; Telser, J. Measuring giant anisotropy in paramagnetic transition metal complexes with relevance to single-ion magnetism. *Dalton Trans.* **2016,** *45*, 16751-16763.

2. Lu, J.; Ozel, I. O.; Belvin, C. A.; Li, X.; Skorupskii, G.; Sun, L.; Ofori-Okai, B. K.; Dinca, M.; Gedik, N.; Nelson, K. A. Rapid and precise determination of zero-field splittings by terahertz time-domain electron paramagnetic resonance spectroscopy. *Chem. Sci.* **2017,** *8*, 7312-7323.

3. Gómez-Coca, S.; Aravena, D.; Morales, R.; Ruíz, E. Large magnetic anisotropy in mononuclear metal complexes. *Coord. Chem. Rev.* **2015,** *289-290*, 379-392.

4. Whangbo, M.-H.; Xiang, H.; Koo, H.-J.; Gordon, E. E.; Whitten, J. L. Electronic and Structural Factors Controlling the Spin Orientations of Magnetic Ions. *Inorg. Chem.* **2019,** *58*, 11854-11874.

5. Boča, R. Zero-field splitting in metal complexes. *Coord. Chem. Rev.* **2004,** *248*, 757-815.

6. Atanasov, M.; Aravena, D.; Suturina, E.; Bill, E.; Maganas, D.; Neese, F. First principles approach to the electronic structure, magnetic anisotropy and spin relaxation in mononuclear 3d-transition metal single molecule magnets. *Coord. Chem. Rev.* **2015,** *289-290*, 177-214.

7. Gatteschi, D.; Sessoli, R. Quantum tunneling of magnetization and related phenomena in molecular materials. *Angew. Chem., Int. Ed.* **2003,** *42*, 268-297.

8. Sessoli, R.; Gatteschi, D.; Caneschi, A.; Novak, M. A. Magnetic bistability in a metal-ion cluster. *Nature* **1993,** *365*, 141-3.

9. Christou, G.; Gatteschi, D.; Hendrickson, D. N.; Sessoli, R. Single-molecule magnets. *MRS Bull.* **2000,** *25*, 66-71.

10. Bogani, L.; Wernsdorfer, W. Molecular spintronics using single-molecule magnets. *Nat. Mater.* **2008,** *7*, 179-186.

11. Leuenberger, M. N.; Loss, D. Quantum computing in molecular magnets. *Nature n***2001,** *410*, 789-793.

12. Friedman, J. R.; Sarachik, M. P. Single-molecule nanomagnets. *Annu. Rev. Condens. Matter Phys.* **2010,** *1*, 109-128.

13. Cahier, B.; Maurice, R.; Bolvin, H.; Mallah, T.; Guihery, N. Tools for predicting the nature and magnitude of magnetic anisotropy in transition metal complexes: application to Co(II) complexes. *Magnetochemistry* **2016,** *2*, 31.

14. Piwowarska, D.; Gnutek, P.; Rudowicz, C. Origin of the Ground Kramers Doublets for $Co^{2+}(3d^7)$ Ions with the Effective Spin 3/2 Versus the Fictitious 'Spin' 1/2. *Appl. Magn. Reson.* **2019,** *50*, 797-808.

15. Gómez-Coca, S.; Cremades, E.; Aliaga-Alcalde, N.; Ruíz, E. Mononuclear Single-Molecule Magnets: Tailoring the Magnetic Anisotropy of First-Row Transition-Metal Complexes. *J. Am. Chem. Soc.* **2013,** *135*, 7010-7018.

16. Zadrozny, J. M.; Long, J. R. Slow Magnetic Relaxation at Zero Field in the Tetrahedral Complex $[Co(SPh)_4]^{2-}$. *J. Am. Chem. Soc.* **2011,** *133*, 20732-20734.

17. Saber, M. R.; Dunbar, K. R. Ligands effects on the magnetic anisotropy of tetrahedral cobalt complexes. *Chem. Commun.* **2014,** *50*, 12266-12269.

18. Craig, G. A.; Murrie, M. 3d single-ion magnets. *Chem. Soc. Rev.* **2015,** *44*, 2135-2147.

19. Murrie, M. Cobalt(II) single-molecule magnets. *Chem. Soc. Rev.* **2010,** *39*, 1986-1995.

20. Feng, M.; Tong, M.-L. Single Ion Magnets from 3d to 5f: Developments and Strategies. *Chem. - Eur. J.* **2018,** *24*, 7574-7594.

21. Bar, A. K.; Pichon, C.; Sutter, J.-P. Magnetic anisotropy in two- to eight-coordinated transition-metal complexes: Recent developments in molecular magnetism. *Coord. Chem. Rev.* **2016,** *308*, 346-380.

22. Tezgerevska, T.; Alley, K. G.; Boskovic, C. Valence tautomerism in metal complexes: Stimulated and reversible intramolecular electron transfer between metal centers and organic ligands. *Coord. Chem. Rev.* **2014,** *268*, 23-40.

23. Boskovic, C. In *Valence tautomeric transitions in cobalt-dioxolene complexes*, John Wiley & Sons Ltd.: 2013; pp 203-224.

24. Shultz, D. A. In *Valence tautomerism in dioxolene complexes of cobalt*, Wiley-VCH Verlag GmbH: 2001; pp 281-306.

25. Pierpont, C. G. Studies on charge distribution and valence tautomerism in transition metal complexes of catecholate and semiquinonate ligands. *Coord. Chem. Rev.* **2001,** *216-217*, 99-125.

26. Caneschi, A.; Gatteschi, D.; Sessoli, R.; Rey, P. Toward molecular magnets: the metal-radical approach. *Acc. Chem. Res.* **1989,** *22*, 392-8.

27. Demir, S.; Jeon, I.-R.; Long, J. R.; Harris, T. D. Radical ligand-containing single-molecule magnets. *Coord. Chem. Rev.* **2015,** *289-290*, 149-176.

28. Gransbury, G. K.; Boulon, M.-E.; Mole, R. A.; Gable, R. W.; Moubaraki, B.; Murray, K. S.; Sorace, L.; Soncini, A.; Boskovic, C. Single-ion anisotropy and exchange coupling in cobalt(II)-radical complexes: insights from magnetic and ab initio studies. *Chem. Sci.* **2019,** *10*, 8855-8871.

29. Wang, J.; Li, J.-N.; Zhang, S.-L.; Zhao, X.-H.; Shao, D.; Wang, X.-Y. Syntheses and magnetic properties of a pyrimidyl-substituted nitronyl nitroxide radical and its cobalt(II) complexes. *Chem. Commun.* **2016,** *52*, 5033-5036.

30. Ma, X.; Suturina, E. A.; De, S.; Negrier, P.; Rouzieres, M.; Clerac, R.; Dechambenoit, P. A Redox-Active Bridging Ligand to Promote Spin Delocalization, High-Spin Complexes, and Magnetic Multi-Switchability. *Angew. Chem., Int. Ed.* **2018,** *57*, 7841-7845.

31. Albold, U.; Bamberger, H.; Hallmen, P. P.; van Slageren, J.; Sarkar, B. Strong Exchange Couplings Drastically Slow Down Magnetization Relaxation in an Air-Stable Cobalt(II)-Radical Single-Molecule Magnet (SMM). *Angew. Chem., Int. Ed.* **2019,** *58*, 9802-9806.

32. Chakarawet, K.; Harris, T. D.; Long, J. R. Semiquinone radical-bridged M_2 (M = Fe, Co, Ni) complexes with strong magnetic exchange giving rise to slow magnetic relaxation. *Chem. Sci.* **2020,** *11*, 8196-8203.

33. Alexandropoulos, D. I.; Vignesh, K. R.; Xie, H.; Dunbar, K. R. Quinoxaline radical-bridged transition metal complexes with very strong antiferromagnetic coupling. *Chem. Commun.* **2020,** *56*, 9122-9125.

34. Jeon, I.-R.; Negru, B.; Van Duyne, R. P.; Harris, T. D. A 2D Semiquinone Radical-Containing Microporous Magnet with Solvent-Induced Switching from $T_c = 26$ to 80 K. *J. Am. Chem. Soc.* **2015,** *137*, 15699-15702.

35. DeGayner, J. A.; Wang, K.; Harris, T. D. A Ferric Semiquinoid Single-Chain Magnet via Thermally-Switchable Metal-Ligand Electron Transfer. *J. Am. Chem. Soc.* **2018,** *140*, 6550-6553.

36. Miller, J. S. Magnetically ordered molecule-based materials. *Chem. Soc. Rev.* **2011,** *40*, 3266-3296.

37. Zhang, X.; Saber, M. R.; Prosvirin, A. P.; Reibenspies, J. H.; Sun, L.; Ballesteros-Rivas, M.; Zhao, H.; Dunbar, K. R. Magnetic ordering in TCNQ-based metal-organic frameworks with host-guest interactions. *Inorg. Chem. Front.* **2015,** *2*, 904-911.

38. Pedersen, K. S.; Perlepe, P.; Aubrey, M. L.; Woodruff, D. N.; Reyes-Lillo, S. E.; Reinholdt, A.; Voigt, L.; Li, Z.; Borup, K.; Rouzieres, M.; Samohvalov, D.; Wilhelm, F.; Rogalev, A.; Neaton, J. B.; Long, J. R.; Clerac, R. Formation of the layered conductive magnet $CrCl_2(pyrazine)_2$ through redox-active coordination chemistry. *Nat. Chem.* **2018,** *10*, 1056-1061.

39. Efthymiou, C.; Winterlich, M.; Papatriantafyllopoulou, C. In *Breakthrough in radical-bridged single-molecule magnets*, Wiley-VCH Verlag GmbH & Co. KGaA: 2018; pp 315-351.

40. Fortier, S.; Le Roy, J. J.; Chen, C.-H.; Vieru, V.; Murugesu, M.; Chibotaru, L. F.; Mindiola, D. J.; Caulton, K. G. A Dinuclear Cobalt Complex Featuring Unprecedented Anodic and Cathodic Redox Switches for Single-Molecule Magnet Activity. *J. Am. Chem. Soc.* **2013,** *135*, 14670-14678.

41. Wang, Y.; Li, J.; Zhang, L.; Chen, C.; Feng, R.; Zhao, Y.; Zhang, Y.-Q.; Tan, G.; Song, Y.; Wang, X. Magnetic on-off switching in redox non-innocent ligand bridged binuclear cobalt complexes. *Dalton Trans.* **2018,** *47*, 17211-17215.

42. Poddel'sky, A. I.; Cherkasov, V. K.; Abakumov, G. A. Transition metal complexes with bulky 4,6-di-tert-butyl-N-aryl(alkyl)-o-iminobenzoquinonato ligands: Structure, EPR and magnetism. *Coord. Chem. Rev.* **2009,** *253*, 291-324.

43. Kaim, W. Manifestations of Noninnocent Ligand Behavior. *Inorg. Chem.* **2011,** *50*, 9752-9765.

44. Fielding, A. J.; Lipscomb, J. D.; Que, L., Jr. A two-electron-shell game: intermediates of the extradiol-cleaving catechol dioxygenases. *J. Biol. Inorg. Chem.* **2014,** *19*, 491-504.

45. Herebian, D.; Bothe, E.; Bill, E.; Weyhermueller, T.; Wieghardt, K. Experimental Evidence for the Noninnocence of o-Aminothiophenolates: Coordination Chemistry of o-Iminothionebenzosemiquinonate(1-) π-Radicals with Ni(II), Pd(II), Pt(II). *J. Am. Chem. Soc.* **2001,** *123*, 10012-10023.

46. Telser, J.; Ozarowski, A.; Krzystek, J. High-frequency and -field electron paramagnetic resonance of transition metal ion (d block) coordination complexes. *Electron Paramagn. Reson.* **2013,** *23*, 209-263.

47. Krzystek, J.; Ozarowski, A.; Telser, J. Multi-frequency, high-field EPR as a powerful tool to accurately determine zero-field splitting in high-spin transition metal coordination complexes. *Coord. Chem. Rev.* **2006,** *250*, 2308-2324.

48. Vongtragool, S.; Gorshunov, B.; Dressel, M.; Krzystek, J.; Eichhorn, D. M.; Telser, J. Direct Observation of Fine Structure Transitions in a Paramagnetic Nickel(II) Complex Using Far-Infrared Magnetic Spectroscopy: A New Method for Studying High-Spin Transition Metal Complexes. *Inorg. Chem.* **2003,** *42*, 1788-1790.

49. Jiang, S.-D.; Haas, S.; Dressel, M.; Bogani, L.; Maganas, D.; Neese, F.; Levesanos, N.; Ferentinos, E.; Kyritsis, P.; Thirunavukkuarasu, K.; Krzystek, J. Direct Observation of Very Large Zero-Field Splitting in a Tetrahedral Ni(II)Se$_4$ Coordination Complex. *J. Am. Chem. Soc.* **2015,** *137*, 12923-8.

50. Kitajima, N.; Fujisawa, L.; Fujimoto, C.; Moro-oka, Y.; Hashimoto, S.; Kitagawa, T.; Toriumi, K.; Tatsumi, K.; Nakamura, A. A New Model for Dioxygen Binding in Hemocyanin. Synthesis, Characterization, and Molecular Structure of the μ-η^2:η^2 Peroxo Dinuclear Copper(II) Complexes, [Cu(HB(3,5-R$_2$pz)$_3$)]$_2$(O$_2$) (R = *i*-Pr and Ph). *J. Am. Chem. Soc.* **1992,** *114*, 1277-1291.

51. Khomenko, T. M.; Salomatina, O. V.; Kurbakova, S. Y.; Il'ina, I. V.; Volcho, K. P.; Komarova, N. I.; Korchagina, D. V.; Salakhutdinov, N. F.; Tolstikov, A. G. New chiral ligands from myrtenal and caryophyllene for asymmetric oxydation of sulfides catalyzed by metal complexes. *Russ. J. Org. Chem.* **2006,** *42*, 1653-1661.

52. Harding, D. J.; Harding, P.; Daengngern, R.; Yimklan, S.; Adams, H. Synthesis and characterization of redox-active tris(pyrazolyl)borate cobalt complexes. *Dalton Trans.* **2009**, 1314-1320.

53. Shaban, S. Y.; Ibrahim, M. M.; Heinemann, F. W. A new sterically loaded pentadentate N3S2 ligand and its zinc complexes. *Inorg. Chim. Acta* **2007,** *360*, 2929-2934.

54. Kumar, P.; Lindeman, S. V.; Fiedler, A. T. Cobalt Superoxo and Alkylperoxo Complexes Derived from Reaction of Ring-Cleaving Dioxygenase Models with O_2. *J. Am. Chem. Soc.* **2019,** *141*, 10984-10987.

55. Bourhis, L. J.; Dolomanov, O. V.; Gildea, R. J.; Howard, J. A. K.; Puschmann, H. The anatomy of a comprehensive constrained, restrained refinement program for the modern computing environment - Olex2 dissected. *Acta Crystallogr., Sect. A: Found. Adv.* **2015,** *71*, 59-75.

56. Sheldrick, G. M. Crystal structure refinement with SHELXL. *Acta Crystallogr., Sect. C: Struct. Chem.* **2015,** *71*, 3-8.

57. Chilton, N. F.; Anderson, R. P.; Turner, L. D.; Soncini, A.; Murray, K. S. PHI: A powerful new program for the analysis of anisotropic monomeric and exchange-coupled polynuclear d- and f-block complexes. *J. Comput. Chem.* **2013,** *34*, 1164-1175.

58. Kahn, O., Molecules Containing a Unique Magnetic Center without First-Order Orbital Momentum. In Molecular Magnetism, VCH Publishers, Inc.: New York, N.Y., 1993; pp. 9–29.

59. Bain, G. A.; Berry, J. F. Diamagnetic corrections and Pascal's constants. *J. Chem. Educ.* **2008,** *85*, 532-536.

60. Hassan, A. K.; Pardi, L. A.; Krzystek, J.; Sienkiewicz, A.; Goy, P.; Rohrer, M.; Brunel, L. C. Ultrawide Band Multifrequency High-Field EMR Technique: A Methodology for Increasing Spectroscopic Information. *J. Magn. Reson.* **2000,** *142*, 300-312.

61. Stoll, S.; Schweiger, A. EasySpin, a comprehensive software package for spectral simulation and analysis in EPR. *J. Magn. Reson.* **2006,** *178*, 42-55.

62. Neese, F. ORCA - An Ab Initio, DFT and Semiempirical Electronic Structure Package, version 4.0, Max Planck Institute for Chemical Energy Conversion, Muelheim (Germany), 2017.

63. Neese, F. The ORCA program system. *Wiley Interdisciplinary Reviews: Computational Molecular Science* **2012,** *2*, 73-78.

64. Weigend, F.; Ahlrichs, R. Balanced basis sets of split valence, triple zeta valence and quadruple zeta valence quality for H to Rn: Design and assessment of accuracy. *Phys. Chem. Chem. Phys.* **2005,** *7*, 3297-3305.

65. Becke, A. D. Density functional thermochemistry. III. The role of exact exchange. *J. Chem. Phys.* **1993,** *98*, 5648-5652.

66. Lee, C. T.; Yang, W. T.; Parr, R. G. Development of the Colle-Salvetti Correlation-energy Formula into a Functional of the Electron Densitry. *Physical Review B* **1988,** *37*, 785-789.

67. Neese, F.; Wennmohs, F.; Hansen, A.; Becker, U. Efficient, approximate and parallel Hartree-Fock and hybrid DFT calculations. A 'chain-of-spheres' algorithm for the Hartree-Fock exchange. *Chem. Phys.* **2009,** *356*, 98-109.

68. Weigend, F. Accurate Coulomb-fitting basis sets for H to Rn. *Phys. Chem. Chem. Phys.* **2006,** *8*, 1057-1065.

69. Angeli, C.; Cimiraglia, R.; Evangelisti, S.; Leininger, T.; Malrieu, J. P. Introduction of n-electron valence states for multireference perturbation theory. *J. Chem. Phys.* **2001,** *114*, 10252-10264.

70. Singh, S. K.; Atanasov, M.; Neese, F. Challenges in Multireference Perturbation Theory for the Calculations of the g-Tensor of First-Row Transition-Metal Complexes. *J. Chem. Theory Comput.* **2018,** *14*, 4662-4677.

71. Singh, S. K.; Eng, J.; Atanasov, M.; Neese, F. Covalency and chemical bonding in transition metal complexes: An ab initio based ligand field perspective. *Coord. Chem. Rev.* **2017,** *344*, 2-25.

72. Atanasov, M.; Ganyushin, D.; Pantazis, D. A.; Sivalingam, K.; Neese, F. Detailed Ab Initio First-Principles Study of the Magnetic Anisotropy in a Family of Trigonal Pyramidal Iron(II) Pyrrolide Complexes. *Inorg. Chem.* **2011,** *50*, 7460-7477.

73. Noodleman, L. Valence bond description of antiferromagnetic coupling in transition metal dimers. *J. Chem. Phys.* **1981,** *74*, 5737-43.

74. Sinnecker, S.; Neese, F.; Noodleman, L.; Lubitz, W. Calculating the electron paramagnetic resonance parameters of exchange coupled transition metal complexes using broken symmetry density functional theory: Application to a Mn(III)/Mn(IV) model compound. *J. Am. Chem. Soc.* **2004,** *126*, 2613-2622.

75. Becke, A. D. Density Functional Calculations of Molecular Bond Energies. *J. Chem. Phys.* **1986,** *84*, 4524-4529.

76. Perdew, J. P. Density functional approximation for the correlation energy of the inhomogeneous electron gas. *Physical Review B* **1986,** *33*, 8822-8824.

77. Fischer, A. A.; Lindeman, S. V.; Fiedler, A. T. Spectroscopic and computational studies of reversible O_2 binding by a cobalt complex of relevance to cysteine dioxygenase. *Dalton Trans.* **2017,** *46*, 13229-13241.

78. Jacobsen, F. E.; Breece, R. M.; Myers, W. K.; Tierney, D. L.; Cohen, S. M. Model Complexes of Cobalt-Substituted Matrix Metalloproteinases: Tools for Inhibitor Design. *Inorg. Chem.* **2006,** *45*, 7306-7315.

79. Addison, A. W.; Rao, T. N.; Reedijk, J.; Vanrijn, J.; Verschoor, G. C. Synthesis, structure, and spectroscopic properties of copper(II) compounds containing nitrogen–sulphur donor ligands; the crystal and molecular structure of aqua[1,7-bis(N-methylbenzimidazol-2′-yl)-2,6-dithiaheptane]copper(II) perchlorate *J. Chem. Soc., Dalton Trans.* **1984**, 1349-1356.

80. Llunell, M.; Casanova, D.; Cirera, J.; Alemany, P.; Alvarez, S. *SHAPE: Program for the Stereochemical Analysis of Molecular Fragments by Means of Continuous Shape Measures and Associated Tools*, version 2.1; Universitat de Barcelona: 2013.

81. Alvarez, S.; Alemany, P.; Casanova, D.; Cirera, J.; Llunell, M.; Avnir, D. Shape maps and polyhedral interconversion paths in transition metal chemistry. *Coord. Chem. Rev.* **2005,** *249*, 1693-1708.

82. Brown, S. N. Metrical Oxidation States of 2-Amidophenoxide and Catecholate Ligands: Structural Signatures of Metal-Ligand π-Bonding in Potentially Noninnocent Ligands. *Inorg. Chem.* **2012,** *51*, 1251-1260.

83. Ruf, M.; Noll, B. C.; Groner, M. D.; Yee, G. T.; Pierpont, C. G. Pocket Semiquinonate Complexes of Cobalt(II), Copper(II), and Zinc(II) Prepared with the Hydrotris(cumenylmethylpyrazolyl)borate Ligand. *Inorg. Chem.* **1997,** *36*, 4860-4865.

84. Mabbs, F. E.; Machin, D. J., *Magnetism and Transition Metal Complexes*. Dover Publications: 2008.

85. Massoud, S. S.; Fischer, R. C.; Mautner, F. A.; Parfait, M. M.; Herchel, R.; Travnicek, Z. Pentacoordinate cobalt(II) complexes with neutral tripodal N-donor ligands: Zero-field splitting for a distorted trigonal bipyramidal geometry. *Inorg. Chim. Acta* **2018,** *471*, 630-639.

86. Massoud, S. S.; Broussard, K. T.; Mautner, F. A.; Vicente, R.; Saha, M. K.; Bernal, I. Five-coordinate cobalt(II) complexes of tris(2-pyridylmethyl)amine (TPA): Synthesis, structural and magnetic characterization of a terephthalato-bridged dinuclear cobalt(II) complex. *Inorg. Chim. Acta* **2008,** *361*, 123-131.

87. Schweinfurth, D.; Sommer, M. G.; Atanasov, M.; Demeshko, S.; Hohloch, S.; Meyer, F.; Neese, F.; Sarkar, B. The Ligand Field of the Azido Ligand: Insights into Bonding Parameters and Magnetic Anisotropy in a Co(II)-Azido Complex. *J. Am. Chem. Soc.* **2015,** *137*, 1993-2005.

88. Schweinfurth, D.; Krzystek, J.; Atanasov, M.; Klein, J.; Hohloch, S.; Telser, J.; Demeshko, S.; Meyer, F.; Neese, F.; Sarkar, B. Tuning Magnetic Anisotropy Through Ligand Substitution in Five-Coordinate Co(II) Complexes. *Inorg. Chem.* **2017,** *56*, 5253-5265.

89. Ruamps, R.; Batchelor, L. J.; Guillot, R.; Zakhia, G.; Barra, A.-L.; Wernsdorfer, W.; Guihery, N.; Mallah, T. Ising-type magnetic anisotropy and single molecule magnet behaviour in mononuclear trigonal bipyramidal Co(II) complexes. *Chem. Sci.* **2014,** *5*, 3418-3424.

90. Shao, F.; Cahier, B.; Guihery, N.; Riviere, E.; Guillot, R.; Barra, A.-L.; Lan, Y.; Wernsdorfer, W.; Campbell, V. E.; Mallah, T. Tuning the Ising-type anisotropy in trigonal bipyramidal Co(II) complexes. *Chem. Commun.* **2015,** *51*, 16475-16478.

91. Shao, F.; Cahier, B.; Riviere, E.; Guillot, R.; Guihery, N.; Campbell, V. E.; Mallah, T. Structural Dependence of the Ising-type Magnetic Anisotropy and of the Relaxation Time in Mononuclear Trigonal Bipyramidal Co(II) Single Molecule Magnets. *Inorg. Chem.* **2017,** *56*, 1104-1111.

92. Shao, F.; Cahier, B.; Wang, Y.-T.; Yang, F.-L.; Riviere, E.; Guillot, R.; Guihery, N.; Tong, J.-P.; Mallah, T. Magnetic Relaxation Studies on Trigonal Bipyramidal Cobalt(II) Complexes. *Chem. - Asian J.* **2020,** *15*, 391-397.

93. El-Khatib, F.; Cahier, B.; Shao, F.; Lopez-Jorda, M.; Guillot, R.; Riviere, E.; Hafez, H.; Saad, Z.; Girerd, J.-J.; Guihery, N.; Mallah, T. Design and Magnetic Properties of a Mononuclear Co(II) Single Molecule Magnet and Its Antiferromagnetically Coupled Binuclear Derivative. *Inorg. Chem.* **2017,** *56*, 4602-4609.

94. Woods, T. J.; Ballesteros-Rivas, M. F.; Gómez-Coca, S.; Ruíz, E.; Dunbar, K. R. Relaxation Dynamics of Identical Trigonal Bipyramidal Cobalt Molecules with Different Local Symmetries and Packing Arrangements: Magnetostructural Correlations and ab inito Calculations. *J. Am. Chem. Soc.* **2016,** *138*, 16407-16416.

95. Schulte, K. A.; Vignesh, K. R.; Dunbar, K. R. Effects of coordination sphere on unusually large zero field splitting and slow magnetic relaxation in trigonally symmetric molecules. *Chem. Sci.* **2018,** *9*, 9018-9026.

96. Mondal, A. K.; Jover, J.; Ruíz, E.; Konar, S. Quantitative Estimation of Ising-Type Magnetic Anisotropy in a Family of C3-Symmetric CoII Complexes. *Chem. - Eur. J.* **2017,** *23*, 12550-12558.

97. Massoud, S. S.; Perez, Z. E.; Courson, J. R.; Fischer, R. C.; Mautner, F. A.; Vanco, J.; Cajan, M.; Travnicek, Z. Slow magnetic relaxation in penta-coordinate cobalt(II) field-induced single-ion magnets (SIMs) with easy-axis magnetic anisotropy. *Dalton Trans.* **2020,** *49*, 11715-11726.

98. Mondal, A. K.; Jover, J.; Ruíz, E.; Konar, S. Investigation of easy-plane magnetic anisotropy in P-ligand square-pyramidal CoII single ion magnets. *Chem. Commun.* **2017,** *53*, 5338-5341.

99. Mondal, A. K.; Goswami, T.; Misra, A.; Konar, S. Probing the Effects of Ligand Field and Coordination Geometry on Magnetic Anisotropy of Pentacoordinate Cobalt(II) Single-Ion Magnets. *Inorg. Chem.* **2017,** *56*, 6870-6878.

100. Nemec, I.; Liu, H.; Herchel, R.; Zhang, X.; Travnicek, Z. Magnetic anisotropy in pentacoordinate 2,6-bis(arylazanylidene-1-chloromethyl)pyridine cobalt(II) complexes with chlorido co-ligands. *Synth. Met.* **2016,** *215*, 158-163.

101. Rajnak, C.; Titis, J.; Salitros, I.; Boča, R.; Fuhr, O.; Ruben, M. Zero-field splitting in pentacoordinate Co(II) complexes. *Polyhedron* **2013,** *65*, 122-128.

102. Brachnakova, B.; Matejova, S.; Moncol, J.; Herchel, R.; Pavlik, J.; Moreno-Pineda, E.; Ruben, M.; Salitros, I. Stereochemistry of coordination polyhedra vs. single ion magnetism in penta- and hexacoordinated Co(II) complexes with tridentate rigid ligands. *Dalton Trans.* **2020,** *49*, 1249-1264.

103. Ghosh, S.; Kamilya, S.; Das, M.; Mehta, S.; Boulon, M.-E.; Nemec, I.; Rouzieres, M.; Herchel, R.; Mondal, A. Effect of Coordination Geometry on Magnetic Properties in a Series of Cobalt(II) Complexes and Structural Transformation in Mother Liquor. *Inorg. Chem.* **2020,** *59*, 7067-7081.

104. Acharya, J.; Sarkar, A.; Kumar, P.; Kumar, V.; Flores Gonzalez, J.; Cador, O.; Pointillart, F.; Rajaraman, G.; Chandrasekhar, V. Influence of ligand field on magnetic anisotropy in a family of pentacoordinate CoII complexes. *Dalton Trans.* **2020,** *49*, 4785-4796.

105. Switlicka, A.; Machura, B.; Penkala, M.; Bienko, A.; Bienko, D. C.; Titis, J.; Rajnak, C.; Boča, R.; Ozarowski, A.; Ozerov, M. Slow Magnetic Relaxation in Cobalt(II) Field-Induced Single-Ion Magnets with Positive Large Anisotropy. *Inorg. Chem.* **2018,** *57*, 12740-12755.

106. Rajnak, C.; Titis, J.; Fuhr, O.; Ruben, M.; Boča, R. Single-Molecule Magnetism in a Pentacoordinate Cobalt(II) Complex Supported by an Antenna Ligand. *Inorg. Chem.* **2014,** *53*, 8200-8202.

107. Mondal, A. K.; Jover, J.; Ruíz, E.; Konar, S. Single-ion magnetic anisotropy in a vacant octahedral Co(II) complex. *Dalton Trans.* **2019,** *48*, 25-29.

108. Hay, M. A.; Sarkar, A.; Craig, G. A.; Bhaskaran, L.; Nehrkorn, J.; Ozerov, M.; Marriott, K. E. R.; Wilson, C.; Rajaraman, G.; Hill, S.; Murrie, M. In-depth investigation of large axial magnetic anisotropy in monometallic 3d complexes using frequency domain magnetic resonance and ab initio methods: a study of trigonal bipyramidal Co(II). *Chem. Sci.* **2019,** *10*, 6354-6361.

109. Hou, X.; Wang, X.; Liu, X.; Wang, J.; Tang, L.; Ju, P. Fine-tuning the effects of auxiliary ligands on two trigonal-bipyramid cobalt(II) complexes exhibiting field-induced slow magnetic relaxation. *New J. Chem.* **2018,** *42*, 8583-8590.

110. Kahn, O., Isotropic Interaction in Dinuclear Compounds. In Molecular Magnetism, VCH Publishers, Inc.: New York, N.Y., 1993; pp. 103–134.

111. Kahn, O., Dipolar, Anisotropic, and Antisymmetric Interactions in Dinuclear Compounds. In Molecular Magnetism, VCH Publishers, Inc.: New York, N.Y., 1993; pp. 135–143.

112. McGarvey, B. R. Theory of the spin Hamiltonian parameters for low spin cobalt(II) complexes. *Can. J. Chem.* **1975,** *53*, 2498-511.

113. Magnetic transitions consistent with our findings were also observed in studies of complexes **1**, **3**, and **4** performed at Helmholtz Zentrum Berlin using frequency-domain Fourier-transform THz-EPR (FD-FT THz EPR). Like FIRMS, FD-FT THz EPR spectroscopy is capable of directly measuring EPR transition energies for complexes with large ZFS, as described in references 114 and 115.

114. Nehrkorn, J.; Telser, J.; Holldack, K.; Stoll, S.; Schnegg, A. Simulating Frequency-Domain Electron Paramagnetic Resonance: Bridging the Gap between Experiment and Magnetic Parameters for High-Spin Transition-Metal Ion Complexes. *J. Phys. Chem. B* **2015,** *119*, 13816-13824.

115. Nehrkorn, J.; Holldack, K.; Bittl, R.; Schnegg, A. Recent progress in synchrotron-based frequency-domain Fourier-transform THz-EPR. *J. Magn. Reson.* **2017,** *280*, 10-19.

116. The **D**-tensors of **1** and **2** are rotated with respect to the molecular coordinate system shown in Figure 8. For both complexes, the *z*-axis of the **D**-tensor lies along the Co–O/S bond.

117. Yamaguchi, K.; Takahara, Y.; Fueno, T. In *Ab-initio molecular orbital studies of structure and reactivity of transition metal-oxo compounds*, Reidel: 1986; pp 155-84.

118. Soda, T.; Kitagawa, Y.; Onishi, T.; Takano, Y.; Shigeta, Y.; Nagao, H.; Yoshioka, Y.; Yamaguchi, K. Ab initio computations of effective exchange integrals for H-H, H-He-H, and Mn2O2 complex: comparison of broken-symmetry approaches. *Chem. Phys. Lett.* **2000,** *319*, 223-230.

119. In references 120 and 121, far-infrared absorption spectroscopy was used to measure the ZFS of bis(dithiolato)cobalt complexes. These complexes are best described as intermediate-spin Co(III) with two closed-shell dithiolato ligands, although DFT calculations suggest that the ligands have partial radical character.

120. Ray, K.; Begum, A.; Weyhermueller, T.; Piligkos, S.; Van Slageren, J.; Neese, F.; Wieghardt, K. The Electronic Structure of the Isoelectronic, Square-Planar Complexes [Fe^{II}(L)$_2$]$^{2-}$ and [Co^{III}(L^{Bu})$_2$]$^-$ (L^{2-} and (L^{Bu})$^{2-}$ = Benzene-1,2-dithiolates): An Experimental and Density Functional Theoretical Study. *J. Am. Chem. Soc.* **2005,** *127*, 4403-4415.

121. Van der Put, P. J.; Schilperoord, A. A. Spin delocalization in square-planar spin-triplet benzene- and toluenedithiolatecobaltate(III). *Inorg. Chem.* **1974,** *13*, 2476-81.

122. Krzystek, J.; Swenson, D. C.; Zvyagin, S. A.; Smirnov, D.; Ozarowski, A.; Telser, J. Cobalt(II) "Scorpionate" Complexes as Models for Cobalt-Substituted Zinc Enzymes:

Electronic Structure Investigation by High-Frequency and Field Electron Paramagnetic Resonance Spectroscopy. *J. Am. Chem. Soc.* **2010,** *132,* 5241-5253.

For Table of Contents Only

Various experimental and computational methods are used to develop magneto-structural correlations for pentacoordinate cobalt(II) complexes consisting of redox-active ligands in multiple oxidation states. The magnetic anisotropies of each complex are measured directly using far-infrared magnetic spectroscopy (FIRMS), and additional electron-structure insights are provided by magnetic susceptibility and high-frequency and -field electron paramagnetic resonance (HFEPR). The experimental results are analyzed within theoretical frameworks provided by density functional and multireference *ab initio* calculations.